THESIS FOR THE DEGREE OF DOCTOR OF PHILOSOPHY IN THERMO AND FLUID DYNAMICS

Turbulence modulation effects caused by small droplets using one-dimensional-turbulence

MARCO FISTLER

Department of Mechanics and Maritime Sciences
CHALMERS UNIVERSITY OF TECHNOLOGY

Gothenburg, Sweden 2020

Turbulence modulation effects caused by small droplets using one-dimensional-turbulence
MARCO FISTLER
ISBN 978-91-7905-350-5

Doktorsavhandlingar vid Chalmers tekniska högskola
Ny serie nr. 4817
ISSN 0346-718X
Department of Mechanics and Maritime Sciences
Chalmers University of Technology
SE-412 96 Gothenburg
Sweden
Telephone: +46 (0)31-772 1000

Cover:
Droplets meet turbulence on ODT line.
Drawn by Annabel Jerre.

Chalmers Reproservice
Gothenburg, Sweden 2020

Turbulence modulation effects caused by small droplets using one-dimensional-turbulence
Thesis for the degree of Doctor of Philosophy in Thermo and Fluid Dynamics
MARCO FISTLER
Department of Mechanics and Maritime Sciences
Chalmers University of Technology

Abstract

This thesis presents a stochastic model to study turbulence modulation effects on gas phases caused by small droplets or more generally speaking particles to achieve a better understanding about the physics and with the aim to provide data for a subgrid-scale (SGS) model for Large-eddy-simulations. The one-dimensional-turbulence (ODT) model addresses one of the major issues for multiphase flow simulations, namely computational costs. It is a dimension-reduced model resolving all turbulent time and length scales and reaching parameter ranges, which are inaccessible for Direct-Numerical-Simulations (DNS). ODT is a stochastic model simulating turbulent flow evolution along a notional one-dimensional line of sight by applying instantaneous maps which represent the effect of individual turbulent eddies on property fields.

For an efficient investigation of turbulence modulation effects, ODT has been extended in this thesis in many ways. First, the Lagrangian particle tracking method developed by Schmidt et al. [1] was modified for spatial, cylindrical flow simulations. Therefore, the two-way coupling mechanism was extended as well. This case serves to study the overall influence of particles on a jet configuration, which conforms with the droplet-laden flow in the dilute region of a spray. Here, the most significant effects are expected. Secondly, a concept for developing a SGS model is presented. Based on this concept, ODT was modified to capture two canonical test cases of stationary, forced isotropic turbulence (HIT) and homogeneous shear turbulence (HST). For this purpose, a forcing scheme that maintains statistical stationarity and a new energy redistribution mechanism during the eddy events are introduced. The latter enables ODT to predict anisotropic turbulent structures. ODT is validated against several data sets of DNS studies and showed its capability to access parameter ranges beyond previous limits. It turned out to have a lot of potential to contribute to a SGS closure of LES for turbulence modulation caused by small droplets.

Keywords: Turbulence, Droplets, Multiphase Flow, one-dimensional-turbulence (ODT)

List of publications

This thesis is based on the work contained in the following publications:

Publication A M. Fistler, D. O. Lignell, A. Kerstein and M. Oevermann, "Numerical study of stochastic particle dispersion using One-Dimensional-Turbulence" in Proceedings of *ILASS-Americas 2017*.

Publication B M. Fistler, D. O. Lignell, A. Kerstein and M. Oevermann, "Numerical studies of turbulent particle-laden jets using spatial approach of one-dimensional turbulence" in Proceedings of *ILASS-Europe 2017*.

Publication C M. Fistler, D. O. Lignell, A. Kerstein and M. Oevermann, "A new LES subgrid-scale approach for turbulence modulation by droplets" in Proceedings of *ICLASS 2018*.

Publication D M. Fistler, D. O. Lignell, A. Kerstein and M. Oevermann, "Turbulence modulation in particle-laden, stationary homogeneous isotropic turbulence using one-dimensional-turbulence" in *Physical Review Fluids 5, 2020*.

Publication E M. Fistler, A. Kerstein, S. Wunsch and M. Oevermann, "Turbulence modulation in particle-laden stationary homogeneous shear turbulence using one-dimensional turbulence" submitted to *Physical Review Fluids* (June 12, 2020).

Additional relevant publication

Publication F D. O. Lignell, V. B. Lansinger, J. Medina, M. Klein, A. Kerstein, H. Schmidt, M. Fistler and M. Oevermann, "One-dimensional turbulence modeling for cylindrical and spherical flows: model formulation and application" in *Theoretical and Computational Fluid Dynamics 32, 2018*.

Acknowledgements

Collaboration and interaction are my main incitements in research and life. It would be impossible for me to sit alone in the basement and contribute to the scientific field. I had the great opportunity to work with some exceptional personalities with diverse perspectives from all over the world, which let me grow so much. Here is not enough space to name everybody who shaped me positively over the last almost 5 years, but I try to point out the most relevant persons related to this work.

As the one who made it all possible in the first place and who is supporting me with all he can, I want to thank Michael Oevermann. He had to handle my frustration due to unsuccessful studies and always had an open-ear for private problems. He guided me and gave me space to grow and to explore on my own. I feel an equal amount of gratitude working together with Alan Kerstein. He spent many hours to consult me on ODT, to make sure I am on track, and to write two journal papers with me I am very proud of.

But five years are not just filled with research, I also had the opportunity to meet people from all over the world due to many business trips or just due to my work environment at Chalmers. I made many friends, who had to listen to a lot of my problems over the years. I especially want to thank Ananda, Amanda, Jelmer, and Guglielmo, who were always there when I had a difficult time.

Without the most important people in my life, I would not have been able to come to Sweden and go the path I am on. All my confidence and determination bases on the security I feel by my parents and brother. They supported all my crazy ideas and always gave me the feeling to be there if it goes wrong. I am so blessed to have you.

To my family.
For giving me wings to fly and
roots to come back to.

Contents

Part I
Extended Summary

1 Introduction

The combustion of liquid fuel accounts for around ∼30% of the total energy production globally [2]. The current big discussions about the electrification of our transportation systems aim almost exclusively at light-duty and partially at heavy-duty vehicles. For marine vessels and airplanes it cannot be foreseen when the technology will be advanced enough to fully replace the combustion propulsion systems. In the near future the freight and passenger market covered by these transportation systems will grow rapidly. The *International Energy Agency* expects till 2050, compared to 2009, twice the transport load covered by trucks, three-fold by ships and four-fold by airplanes [3]. The growth will result in an inevitable environmental impact, which can be relaxed by the improvement of the combustion systems towards efficiency increase and pollution reduction. The Drawdown project, which ranks the impact of solutions reaching the goal to stay below 2°C of global warming, quantifies the required reduction of CO_2 emissions of trucks, ships and airplanes by in total 15.28 Gigatones in the next 30 years [4].

The demand for improvements is also forced by emission legislations of the European Union and other governmental institutions. Therefore, emission reduction is a key priority of the industry and has achieved big steps in the last decades, especially towards NOx and soot emissions. Despite the economic power and effort the advancement of fuel injection systems, which mainly governs the combustion process, is still compromised by an incomplete understanding of the physical mechanisms. The work conducted in this thesis was part of a European Union Horizon 2020 initiative to develop a "Holistic Approach of Spray Injection through a generalized multi-phase framework".

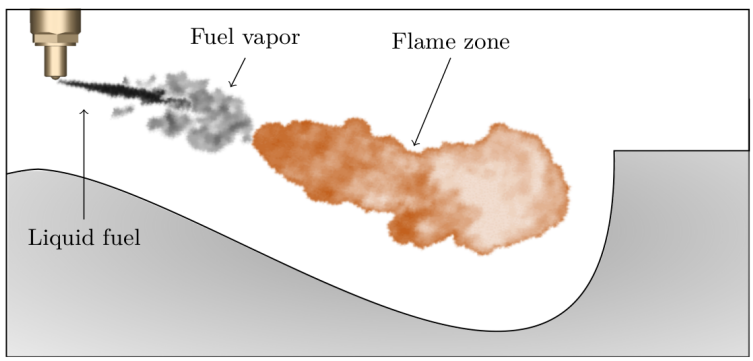

Figure 1.1: *Fuel injection in piston engine (Pictures of spray and flame by Du [5])*

Sprays

Fig. 1.2 displays a schematic sketch of the spray regimes and their dominant physical mechanisms. It starts with the in-nozzle flow, which is mainly governed by the pressure

differences between nozzle inlet and the in-nozzle geometry. Inside the nozzle, *cavitation* can occur which leads to a partial reduction of the effective nozzle diameter. This affects flow and turbulence properties and influences the jet atomization regimes and mechanisms downstream. Behind the nozzle exit, the liquid jet issues into stagnant air, which has a much lower pressure and density. After exiting the nozzle the liquid phase has a dense liquid core, which first breaks up into larger ligaments and then into smaller droplets. The regime, where the first ligaments or droplets are shed from the liquid core, is called *primary atomization*. The subsequent break-up process by which these ligaments or droplets are getting smaller due to inertial effects of the gas phase is called *secondary atomization*. In this regime the now really small droplets are evaporating and form a fuel-gas cloud around the spray, which can be ignited. In the transition zone between the regimes of secondary atomization and evaporation, the spray becomes dilute, i.e. the volume ratio of liquid to gas phase is below 10^{-2}, and the momentum and energy exchange between the small droplets and the gas phase turbulence becomes equally significant for both phases. Before the droplet phase dominated the momentum and energy balance and later the gas turbulence governs the mixing process. However, in between the internia of the droplets in the dilute region modulates the gas turbulence and, when transported downstream, effects the fuel-air mixing process and so the flame regime. As an accurate prediction of the flame regime is crucial to provide reliable data to increase the effiency of the whole process, this dilute spray interaction plays an important role in this chain reaction. The investigation of this interaction and its governing mechanisms is the scope of this thesis.

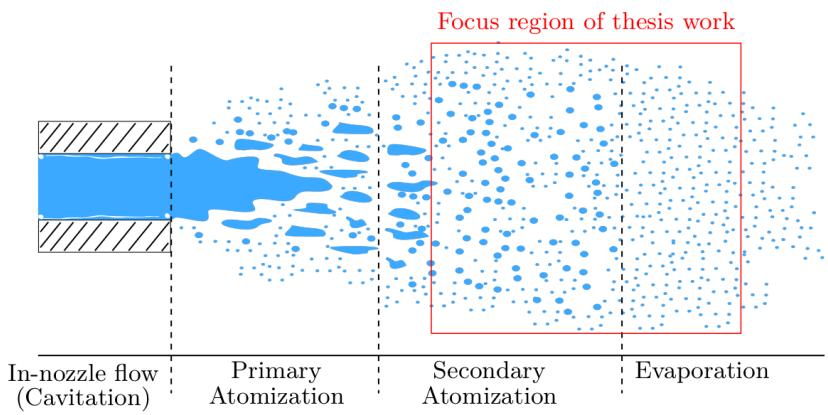

Figure 1.2: *Sketch of liquid spray regimes and its dominant mechanisms*

Turbulence modulation

The effect of droplets, in the focus region (marked in Fig. 1.2) assumed to be similar to rigid, spherical particles, on the gas phase turbulence is called turbulence modulation. Despite the fact that the first research in the field of dispersed two-phase flows can be traced back to the 17th century by Stevin and Newton, the biggest issue remains even today the understanding of turbulence itself [6]. Even with modern experimental equipment and high-performance computational flow simulations it is still challenging to capture the turbulence quantities of both phases at the same time.

CFD (computational fluid dynamics) proved to be a powerful tool to investigate dispersed two-phase flows and to acquire detailed flow information. However, many CFD approaches for these flow types have limited predictive capabilities or rely on many assumptions, which affects the accuracy and restricts their generality. Direct Numerical Simulations (DNS), which resolve all scales, are limited to low turbulent cases due to their high computational costs and mainly focus on academic test cases. Large-Eddy-Simulations resolve only the large scales and provide currently the most sophisticated method to simulate flows in complex geometries like an internal combustion engine. However, the smaller, unresolved scales are predicted by so-called subgrid-scale (SGS) models and for many multiphase phenomena these models are lacking accuracy or overall existence. This also counts for turbulence modulation effects and, thus, this thesis is about an alternative approach to support the development towards a reliable SGS model for turbulence modulation effects.

One-Dimensional-Turbulence

In this thesis an alternative approach called One-Dimensional-Turbulence (ODT) is used, which was introduced in [7] and extended by several international research groups over the last two decades. ODT has demonstrated to predict topologically simple flows such as boundary layers and jets, with large property gradients in one direction, very well compared to DNS studies and experimental data. This stochastic model is used here to tackle one of the major problems for multiphase flow simulations, namely computational costs, with the goal to predict statistical properties of these types of flow more efficiently. By reducing the costs, it will be possible to investigate parameter ranges with ODT which are not accessible for DNS. By investigating these ranges it is aimed to provide subsequently a subgrid-model for LES based on gathered ODT data. In a related multiphase application, Movaghar et al. [8, 9] showed the ability of ODT to model primary breakup in a turbulent jet application. Schmidt et al. [1] and Sun et al. [10, 11] extended the ODT model to predict fluid-particle interactions. As part of this thesis the model is further extended and tested in different flow conditions and representations. A first attempt loading a spatial, cylindrical representation of a jet flow with particles is followed by the more general temporal test cases of forced stationary, homogeneous isotropic turbulence (HIT) and homogeneous shear turbulence (HST).

Summarizing, the aim of this thesis is to study turbulence modulations effects on the gas phase caused by small-droplets using ODT to provide additional insights for parameter ranges not accessible with other numerical approaches. Additionally, these new insights should contribute to the development of a SGS closure of LES.

The thesis is structured as follows. After the introduction in this chapter, the physical fundamentals of turbulent flows, small droplets, and their interaction with each other are presented in Chapter 2. It also shows the expected parameter ranges in the far field region of the spray. Then, Chapter 3 and 4 introduce the ODT model and its Lagrangian particle tracking method, respectively. Chapter 5 outlines the extensions of the ODT model and bring them into perspective with the investigations done in this thesis. A short summary of the published work is presented in Chapter 6. Chapter 7 concludes and gives an outlook to potential future studies.

2 Physical Fundamentals

In this chapter some features of turbulence, droplet evolution, and their interaction are summarized. Very detailed descriptions of these phenomena can be found in standard textbooks such as Pope [12] (turbulence), Clift et al. [13] (droplets) and Crowe et al. [14] (both), but the important theoretical statements are summarized here for later consideration.

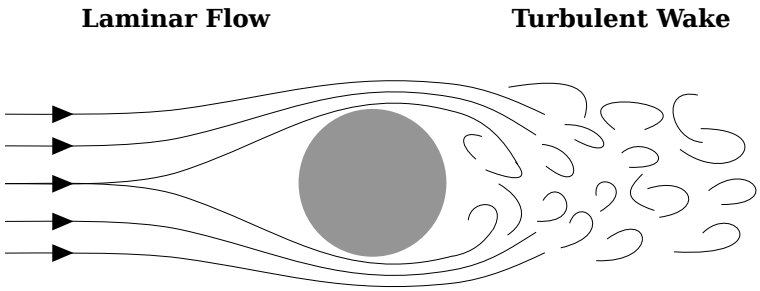

Figure 2.1: *Flow around a cylinder with a turbulent wake*

2.1 Turbulence

In a combustion engine (e.g. a gas turbine or a diesel engine) the fuel is injected into the combustion chamber by a high pressure drop, which results in a very high injection velocity. This is necessary to provide enough fuel in a short time frame and for a sufficient mixture of fuel and air. Due to the high velocity, the liquid phase (fuel) is already turbulent when it exits the injector nozzle. But also the air flow around the liquid phase will become turbulent as a result of the high velocity gradients between the phases. These turbulent effects are causing deformations on the liquid phase and govern the break-up processes. The same phenomena occurs if turbulence interacts with smaller droplets until they are small enough to evaporate. But what is turbulence and how can it be quantified?

Turbulence is seen as a three-dimensional chaotic instability of flow properties caused by an increase of inertial forces relative to viscous damping. Above a critical value of the ratio between inertial and viscous forces a flow configuration is called turbulent (see Fig. 2.1). This knowledge goes back to the famous experiment of Osborne Reynolds (1883), where he found out that the occurrence of instabilities in a flow can be characterized by a single non-dimensional parameter. The parameter is called the Reynolds number and is given as $Re = \frac{L \cdot u}{\nu}$, where L and u are characteristic integral length, e. g. cylinder diameter, and velocity scales, respectively, describing the inertial effects, while ν denotes the kinematic viscosity. For different flow configurations, different critical Reynolds numbers exist which are seen as a boundary between laminar and turbulent flow. For example,

in case of a flow around a sphere the integral length scale is given by the sphere diameter and the characteristic velocity as the relative velocity between the sphere and the flow.

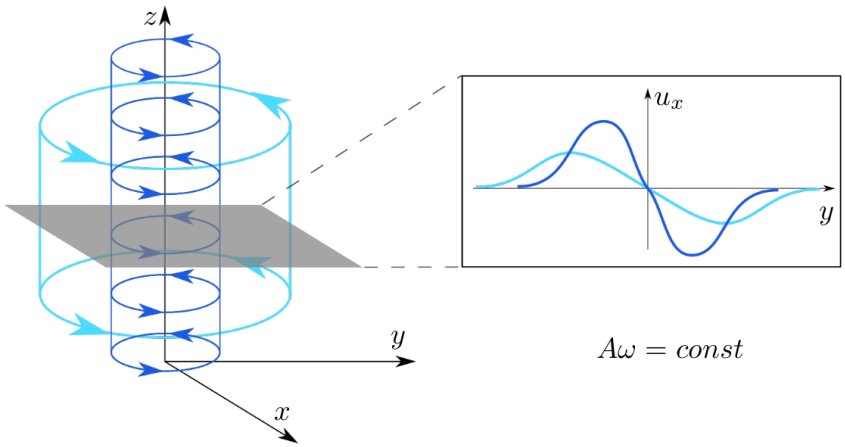

Figure 2.2: *Vortex stretching model by Bradshaw [15].*

In theory the instantaneous turbulent movement is seen as always rotational. Based on Helmholtz's theorems for gas motion in vortex filaments, Bradshaw [15] described turbulence as a vortex stretching process. If we consider a Cartesian coordinate system (x,y,z) and a vortex filament along the z-axis, it is rotating in the xy-plane (Fig. 2.2). By stretching the vortex filament in z direction its cross-section will get smaller and due to the conservation of angular momentum, which is given as product of angular speed times cross-section, the angular speed will increase. This means that an extension in one direction decreases the length scale (cross-section or radius of the cross-section) and speeds up the velocity components in the other two directions. This in turn stretches other elements of the gas with vorticity components in these directions [15], which results in a "cascade" of stretching processes with decreasing length scales. Summarized, the mechanism of vortex stretching shows that turbulence is distributing velocity fluctuations along all three components over all possible length scales. The range of length scales is limited by flow specific boundary conditions and viscosity, which define the Reynolds number. The viscosity is smoothing large velocity gradients and determines the smallest possible length scale, called Kolmogorov scale, before kinetic energy dissipates into thermal internal energy.

Going from the conceptual depiction to a mathematical, deterministic formulation, we assume the *Navier-Stokes* equations as the most accurate equation to capture the behavior of a continuous fluid motion on a macroscale level. For an incompressible, Newtonian fluid with a constant density, they are given as

$$\frac{\partial u_i}{\partial x_i} = 0 \tag{2.1}$$

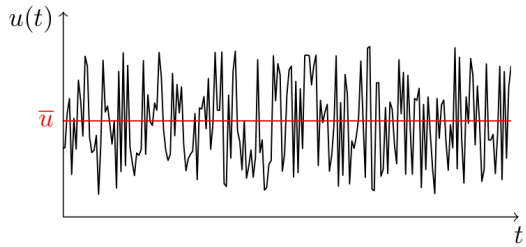

Figure 2.3: *Velocity signal over time in a turbulent flow*

$$\rho\frac{\partial u_i}{\partial t}+\rho\frac{\partial u_i u_j}{\partial x_j}=\frac{\partial p}{\partial x_i}+\mu\frac{\partial^2 u_i}{\partial x_j \partial x_j}. \tag{2.2}$$

The dynamic viscosity μ is given as $\mu = \nu\rho$. Due to the appearance of instabilities in turbulent flows they can be seen in some cases as multiplexed three-dimensional, stochastic fluctuations over a steady flow structure. Fig. 2.3 shows the axial velocity signal in a turbulent flow at a fixed position. Turbulence includes a randomness, which means its exact values are unpredictable. Hence, statistical tools are helpful treating the velocity values as a random process and representing its turbulent structure by statistical moments. Therefore, the velocity value is decomposed in an averaged mean component $\bar{u}$ and a randomly fluctuating part u': $u = \bar{u} + u'$. This decomposition is known as *Reynolds decomposition*. Depending on the gathered data different averaging procedure can be applied, e.g. temporal, spatial or Ensemble average. Using the time averaged Reynolds decomposition in Eqs. 2.1 and 2.2 and summarizing all terms, we get the *Reynolds Averaged Navier-Stokes* (RANS) equations, given as

$$\frac{\partial \bar{u}_i}{\partial x_i}=0 \tag{2.3}$$

$$\bar{\rho}\frac{\partial \bar{u}_i \bar{u}_j}{\partial x_j}=\frac{\partial \bar{p}}{\partial x_i}+\frac{\partial}{\partial x_j}\left(\mu\frac{\partial \bar{u}_i}{\partial x_j}-\rho\overline{u_i' u_j'}\right). \tag{2.4}$$

The new appearing term $\overline{u_i' u_j'}$ on the right hand side of Eq. 2.4 is called the *Reynolds stress tensor* and represents correlations between fluctuating velocities [16]. The diagonal components ($i = j$) are the *normal stresses*, while the off-diagonal components ($i \neq j$) are *shear stresses*. If all statistic moments are independent of its direction, which results in equal values of the normal stresses, the flow is called *isotropic*. The first important indicator for the overall turbulence level in a flow is the *turbulent kinetic energy* k, which is defined as half the trace of the Reynolds stress tensor as

$$k=\frac{1}{2}\overline{u_i' u_i'}. \tag{2.5}$$

The transport equation [12] for k is given as

$$\frac{\partial k}{\partial t}+\bar{u}_j\frac{\partial k}{\partial x_j}=\mathcal{P}-\epsilon, \tag{2.6}$$

where the production term $\mathcal{P}$ is

$$\mathcal{P} = -\overline{u_i' u_j'} \frac{\partial \bar{u}_i}{\partial x_j} \tag{2.7}$$

and the dissipation rate ϵ is

$$\epsilon = -\nu \overline{\frac{\partial u_i'}{\partial x_j} \frac{\partial u_i'}{\partial x_j}}. \tag{2.8}$$

Here, we omitted the diffusion and buoyancy terms for simplicity. These three quantities k, $\mathcal{P}$, ϵ play the key roles defining the turbulent characteristics of a flow.

Following the concept of a turbulent cascade, we assume the flow consists of a spectrum of different eddy sizes. Using Fourier series to analyze the turbulent fluctuations, seen in Fig. 2.3, the turbulent scales are distributed over a range of scales extending from the largest scales, which interact with the mean flow, to the smallest scales, where dissipation occurs [16]. Each of these scales has a certain kinetic energy, which can be studied in wave number κ space and expressed as

$$E(\kappa) d\kappa. \tag{2.9}$$

The integral over the whole wavenumber space gives then the turbulent kinetic energy (TKE) k, i.e.

$$k = \int_0^\infty E(\kappa)\, d\kappa. \tag{2.10}$$

In isotropic turbulence, this typically leads to a spectrum sketched in Fig. 2.4, so-called Kolmogorov spectrum.

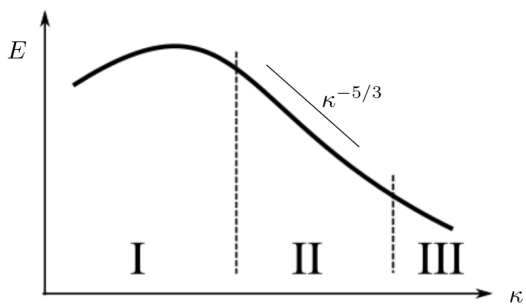

Figure 2.4: *Sketch of a Kolmogorov spectrum for turbulent kinetic energy in isotropic turbulence. I: Energy containing range. II: Inertial subrange. III: Range of small, isotropic scales. [16]*

The Kolmogorov spectrum is generally segmented in three regions, which are governed by different physical mechanisms. The first range (I) contains the large scales with the most energy carried. Here, the mean flow plays the key role and governs the energy transfer mainly with the production term $\mathcal{P}$. The other end of the spectrum (range III) is the so-called *dissipation range*, where the eddies are small and isotropic. Here, the energy

transfers from TKE to thermal energy. The process is governed by ϵ. The second range is the so-called *inertial subrange*, whose length increases for increasing Reynolds number. In this range the energy is transferred between the production scales and the dissipative scales and forms the *cascade process* mentioned before. A flow with stationary turbulence level k implies $\mathcal{P} = \epsilon$, which means production of energy coming from the mean flow is in balance with the amount of k which dissipates at the small scales.

As the large scales are mainly governed by the flow configuration and its boundary conditions, the small scales are assumed to have a universal characteristics. Kolmogorov [17], in addition to Richardson's work [18], formulated three hypothesis regarding them.

Lemma 1: Local isotropy

- At sufficiently high Reynolds number, the small scale turbulent motions (range III) are statistically isotropic.

Lemma 2: First similarity hypothesis

- In every turbulent flow at sufficiently high Reynolds number, the statistics of the small-scale motions range III) have a universal form that is uniquely determined by ν and ϵ.

Lemma 3: Second similarity hypothesis

- In every turbulent flow at sufficiently high Reynolds number, the statistics of the motions of scale l in the range between largest and smallest scales (range II) have a universal form that is uniquely determined by ϵ, independent of ν.

Based on Lemma 2, we can form by dimensional analysis the unique Kolmogorov length, velocity and time scales:

$$\eta = (\nu^3/\epsilon)^{1/4} \tag{2.11}$$

$$u_\eta = (\nu\epsilon)^{1/4} \tag{2.12}$$

$$\tau_\eta = (\nu/\epsilon)^{1/2}. \tag{2.13}$$

These quantities characterize the smallest, dissipative eddies.

Nonetheless, among others three important scales exist to define characteristics for the other two ranges. Many flows in nature or industry are bounded by walls and geometries which they surround. The largest energy containing scales, also called *integral length scales*, are constraint by the length of these boundaries. In academic cases like a cube of homogeneous, isotropic turbulence or homogeneous shear turbulence the flow is generally speaking not bounded and it requires a mathematical formulation to define the characteristic length and time scale which produces TKE. The integral length and time scales, L_{11} and T_{11}, are defined as

$$L_{11} = \frac{\pi}{2u'^2} \int_0^{\kappa_{max}} \frac{E(\kappa)}{\kappa}\, d\kappa, \qquad T_{11} = \frac{L_{11}}{u'}, \tag{2.14}$$

where $E(\kappa)$ is the TKE for each spatial frequency and u' is the average fluctuation given as $u' = \sqrt{\frac{2}{3}k}$.

The last length scale presented here is the *Taylor microscale*. Its definition bases on the longitudinal velocity autocorrelation function and a parabola intersecting the axis for the distance. It is an intermediate length scale between integral and dissipative length scale at which the viscosity significantly affects the dynamic of turbulent eddies. As its detailed derivation is out of the scope (we refer to Pope [12]), a short summary of its features is helpful here. First, the Taylor microscale [19] is given as,

$$\lambda = \sqrt{10\nu k/\epsilon}. \tag{2.15}$$

Despite its original, incorrect definition to give the smallest scales before dissipation, it is commonly used as the length scale between L_{11} and η at high Reynolds numbers. Even without a clear physical interpretation, it is often used and a well-defined quantity for grid-turbulence in form of the Taylor-scale Reynolds number

$$Re_\lambda = \frac{u'\lambda}{\nu}. \tag{2.16}$$

An additional important role plays the pressure variance $p\prime$ in incompressible, anisotropic turbulent flows. Considering the transport equation for the Reynolds stresses $\overline{u_i' u_j'}$ derived from the Navier-Stokes equations

$$\frac{\partial}{\partial t}\overline{u_i' u_j'} + \frac{\partial}{\partial x_k}\overline{u_i' u_j' u_k'} = \nu\frac{\partial^2 \overline{u_i' u_j'}}{\partial x_i \partial x_j} + \mathcal{P}_{ij} + \Pi_{ij} - \epsilon_{ij}, \tag{2.17}$$

where $\mathcal{P}_{ij}$ and ϵ_{ij} represent the production and dissipation tensor, respectively. A special focus is on the velocity-pressure-gradient tensor

$$\Pi_{ij} = -\frac{1}{\rho}\overline{u_i\frac{\partial p'}{\partial x_j} + u_j\frac{\partial p'}{\partial x_i}}. \tag{2.18}$$

Pope [12] showed that Π_{ij} plays a central role in turbulent boundary-layer flows to redistribute TKE among all components. In these flows where $\partial u_1/\partial y$ is the only significant mean velocity gradient, this term extracts energy from $\overline{u_1'^2}$ and transfer it to $\overline{u_2'^2}$ and $\overline{u_3'^2}$. This phenomena is called *pressure-scrambling* and aims to lead the flow to return-to-isotropy. This phenomena can be interpreted separately from the pressure gradient term in Eq. 2.4. The latter has only a contribution to the mean flow.

2.2 Droplets and Particles

Before we investigate the behavior of multiple droplets in a turbulent flow, it is important to understand first the fundamental behavior of a single droplet in a surrounding turbulent flow field. Therefore, we assume common (simplified) properties for each droplet. In the following section, the shape, equation of motion and coupling effects between both phases are discussed with its required assumptions and simplifications.

2.2.1 Shape

Initially, it is essential for the aerodynamic effects to define the shape of droplets. The range of droplet shapes is limited compared to solid particles, due to its smooth surface caused by surface tension effects, but can change dynamically. Often, they occur axisymmetric and, under special circumstances, spherical. The rule-of-thumb to term droplets as spherical is if the minor to major axis ratio is smaller than 10% [13]. Fig. 2.5 shows a regime diagram of droplet shapes depending on the non-slip Reynolds number (Re_p) and the Weber number (We), which are given as

$$Re_p = \frac{\rho_g \Delta v d_p}{\mu}, \quad We = \frac{\rho_g (\Delta v)^2 d_p}{\sigma_p}. \tag{2.19}$$

The subscripts p and g are representing the dispersed (droplet) phase and the gas phase, respectively. ρ, μ and σ_p are the density, viscosity and surface tension, respectively. Δv is the relative velocity between droplet and gas phase $|\vec{v}_p - \vec{v}_g|$ and d_p is the droplet diameter. v is used instead of u to denote velocities because the velocities used to advance the particles are not necessarily the same as for the gas phase velocities u_i.

Re_p describes the ratio between inertial to viscous forces. We is a measure of the relative importance of the gas's inertia compared to its surface tension. As we are investigating non-reacting flows at low temperatures the surface tension of diesel and other common fuels in sprays lies in a range of 20-30$\cdot 10^{-3}$ N/m for these conditions. Droplets sizes in the far field region of a spray are relatively small and range from order of 10^{-4}m to 10^{-6}m [20]. Additionally, the relative velocity between droplets and gas phase is assumed to be very small due to its small response time (see Chapter 2.2.2). Considering these estimations we assume for the following considerations to be in the regime of spherical shapes without expecting shape changes or break-ups. Thus droplets are deemed as spherical rigid particles.

2.2.2 Equation of Motion

Investigating the behavior of a suspended, rigid sphere in a turbulent flow is in the scientific scope since centuries. It started with Stokes analytical solution for creeping flows ($Re_p < 1$) (1851) [22] and improvement suggestions by Oseen (1910) [23] and Lamb (1911) [24]. Using their basic ideas for relatively low Reynolds numbers several groups extended them resulting in the most commonly used approximation for a sphere

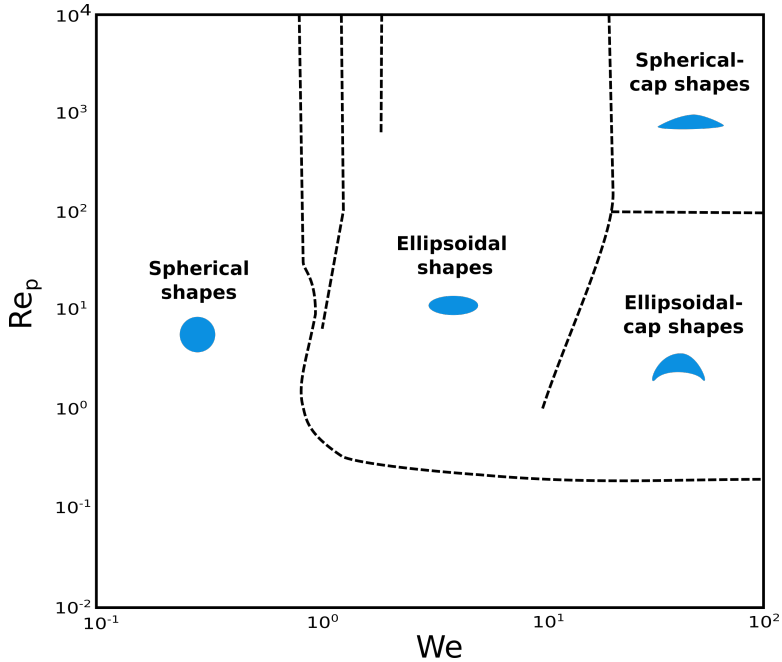

Figure 2.5: *Shape regimes for droplets depending on Weber (We) and Reynolds (Re_p) number.(Adopted from Loth [21])*

in an unsteady flow, which is the so-called Basset-Boussinesq-Oseen (BBO) equation. It summarizes all forces on a sphere in a non-stationary gas and after several updates and corrections by Tchen (1947) and Maxey and Riley (1983) the current equation was derived as

$$m_p \frac{dv_{p,i}}{dt} = F_G + F_P + F_{aM} + F_D + F_B. \tag{2.20}$$

The equation consists of five terms on the right hand side which can be interpreted as gravitational (F_G), pressure gradient (F_P), added mass (F_{aM}), Stokes drag (F_D) and Basset (F_B) forces. The main assumptions, under which the equation is valid, are that the non-slip Reynolds number is smaller than unity and the particle size is smaller than the smallest structure of the flow (Kolmogorov scale [25]). Additionally, the density ratio between gas and particle phase must be high. Therefore, the particle can be seen as a point force located at the center of mass. Due to the assumptions stated above the flow is assumed to be symmetrical and uniform around the particle, so the BBO equations does not consider lift effects and the higher order terms of Eq. 2.20 can be neglected [6]. Also, if the density of the particle is assumed to be larger than the gas phase density, Eq. 2.20 leads to a simplified version only taking into account the dominating gravitational and drag forces, which leads to

$$m_p \frac{dv_{p,i}}{dt} = m_p g_i - 3\pi d_p \eta (v_{p,i} - v_{f,i}). \tag{2.21}$$

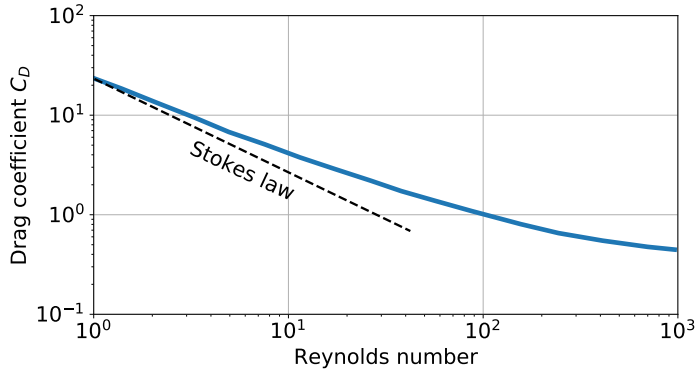

Figure 2.6: *Drag coefficient of a sphere depending on non-slip Reynolds number (standard drag curve) [26]*

The drag force term for an arbitrary shape is given as $F_D = \frac{1}{2}\rho_g(v_{p,i} - v_{f,i}) \cdot A \cdot C_D$, where A is the cross-section normal to the velocity component and C_D is the drag coefficient. Based on the first experiments by Stokes the drag coefficient were derived to $C_D = \frac{24}{Re_p}$, which leads to the second term on the right hand side of Eq. 2.21. By taking a look at the standard drag curve in Fig. 2.6 we see a discrepancy for $Re_p > 1$. Schiller and Naumann [27] derived an empirical correction factor (f) for non-slip Reynolds number smaller than 200. It is given as

$$f = (1 + 0.15Re_p^{0.687}). \tag{2.22}$$

Adding f to Eq. 2.21 and dividing by the mass of a spherical particle we get

$$\frac{dv_{p,i}}{dt} = g_i - \frac{18\nu\rho_f}{d_p^2\rho_p} \cdot f \cdot (v_{p,i} - v_{g,i}). \tag{2.23}$$

Eq. 2.23 will be the starting point for the Lagrangian Particle model in the one-dimensional-turbulence framework (Chapter 3).

As the factor $\frac{18\nu\rho_f}{d_p^2\rho_p}$ has the dimensions s^{-1} it can be interpreted as the inverse of the time a particle needs to reach the velocity of the surrounding gas. It is the so-called Stokes time scale or particle relaxation time τ_p. Its influence is shown in Fig. 2.7 on a simplified model problem. Here, the gas velocity v_g is a sine curve, $v_p(t = 0) = 0$ and $g = 0$. Then, we advanced Eq. 2.23 by using a first-order Euler scheme. τ_p can be interpreted as the reaction time a particle needs to reach the gas velocity. Thus, in the model problem smaller τ_p is closer to the gas phase velocity than the larger τ_p.

An important parameter for particle-turbulence interaction is the ratio of particle relaxation time (τ_p) to a characteristic flow time scale, the so-called Stokes number (St). In this study the characteristic flow time scale will be the Kolmogorov time scale [25], which can be estimated by

$$\tau_\eta = \sqrt{\frac{\nu}{\epsilon}}, \tag{2.24}$$

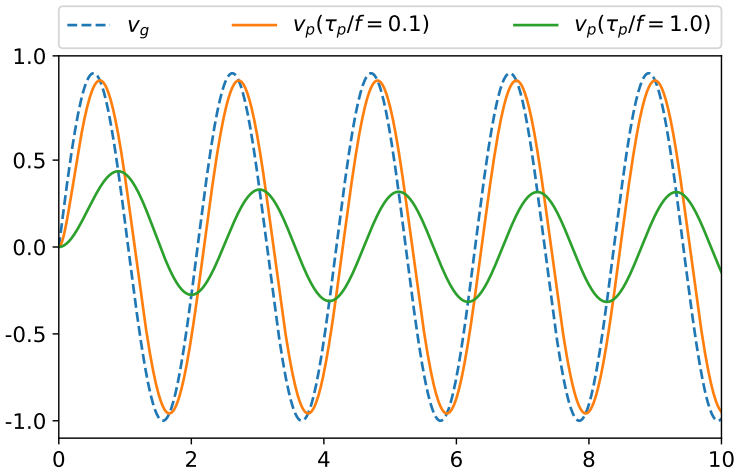

Figure 2.7: *Velocities of the gas v_g and particle v_p phase, for different τ_p, using a model problem, where the gas velocity is predefined as sine curve.*

where ϵ is the dissipation rate of turbulent kinetic energy. This leads to

$$St = \frac{\tau_p}{\tau_\eta}. \tag{2.25}$$

The Stokes number St represents the ratio of inertial forces of the particle compared to the inertial force of the turbulent gas phase. St is commonly used as a dominant parameter to define the interaction regime of turbulence and particles.

2.2.3 Coupling effects

In a spray application multiple droplets interact with the gas phase and require different model approaches depending on the ratio of each occupied volume. The interacting effects between particle and gas phase are classified in three groups based on the volume load, which is defined as a ratio of the volume occupied by the particles to the total volume (Elghobashi [28]),

$$\alpha = \frac{V_{dispersed}}{V_{tot}}. \tag{2.26}$$

In reality the two phases are interacting with each other and additionally the particles can collide with each other. Capturing all interactions is very costly and, thus, it is relevant to define regimes in which we can neglect some of the effects.
For the *one-way coupling* the momentum of the gas phase is coupled with the motion of the dispersed phase. The back-coupling effect is neglected. This is sufficient if the volume loading is in an order of 10^{-6}-10^{-5} depending on the density ratio [28]. Above these values, the energy and momentum transfer from the dispersed phase back to the gas phase

increases significantly and requires a so-called *two-way coupling*. Hence, both transport equations have to be solved in parallel and the governing gas phase equation contains a additional source term. If the volume loading increases further and the dispersed phase can not be characterized as diluted any more, collision or hydrodynamic interactions can occur between the particles (*four-way coupling*). In the literature [28], this regime starts from a volume loading of 10^{-2}. However, more parameters are playing a key role here, e.g. the relative velocity of the particles to the gas phase.

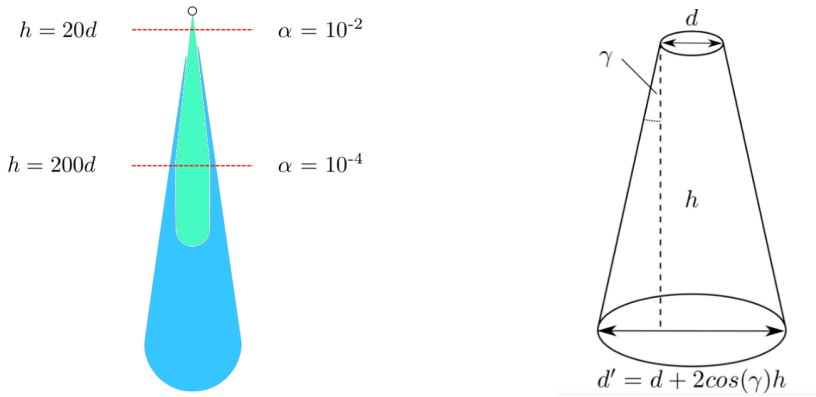

(a) (b)

Figure 2.8: *Determination of volume loading in a spray. a) shows a representation of liquid(green) and vapor(blue) phase of a spray (adopted from Du [5]) and the regime boundaries for two- and four-way coupling. b) shows a sketch to determine the volume loading α by weighting the inlet area ($A = \frac{\pi}{4}d^2$) to the area downstream depending ($A' = \frac{\pi}{4}d'^2$) on the spray cone angle γ.*

For spray applications the volume loading can be estimated by considering the spray dispersion as a cone geometry and taking the ratio of the nozzle outlet area with diameter d to the cross-section area further down stream with diameter d' (see Fig. 2.8). We assume that at the outlet the cross-section is only occupied by liquid fuel. To determine the distance from where we can assume a two-way coupling, the spray cone angle γ is necessary to be known. Based on data of an experimental study of a diesel spray by Du [5], we assume a constant spray angle $\gamma = 15°$. After using trigonometric relations and considering a very small axial distance Δx, the volume loading is assumed as,

$$\alpha = \frac{V}{V'} = \frac{A\Delta x}{A'\Delta x} = \frac{\pi}{4}\frac{4}{\pi}\frac{d^2}{d'^2} = \frac{d^2}{(d + 2\cos(\gamma)h)^2}. \tag{2.27}$$

Solving Eq. 2.27 for h gives,

$$h = \frac{d}{2\cos(\gamma)}\left(\frac{1}{\sqrt{\alpha}} - 1\right). \tag{2.28}$$

Here, the two-way coupling approach is valid after a distance of $\sim 20d$ using the regime

boundary $\alpha = 10^{-2}$. Commonly, the injector diameter d is of order 10^{-4}m. As the scope of this thesis is the area after the atomization regimes, this assumption is reasonable and collision effects can be neglected.

Due to the developing steps of the Lagrangian tracking method, a first study was made assuming a one-way coupling effect. For tracking a single particle this assumption is sufficient. The following studies focused on the two-way coupling approach, as the mass loading is in the range 0.5 to 1, corresponding to a volume loading range $2{\cdot}10^{-4}$ - $4{\cdot}10^{-4}$.

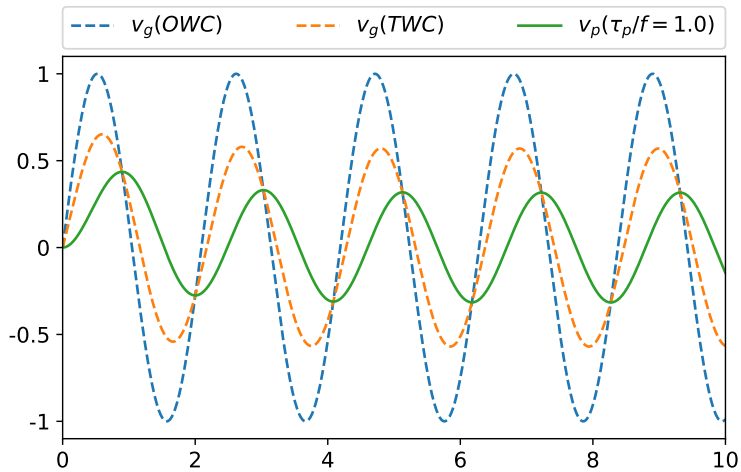

Figure 2.9: *Influence of the two-way coupling mechanism on the gas velocity in a simplified model problem (same as Fig.2.7).*

For getting a visual idea of the two-way-coupling mechanism, the simplified model problem of the gas velocity as a sine curve (shown in Fig. 2.7) is modified with the back coupling effect in Fig. 2.9. Therefore, we subtract the changed particle momentum, during time advancement of Eq. 2.23, from the gas phase momentum assuming a significant particle mass to see the effect. Here, the damping effect of the gas velocity, which can represent a velocity fluctuation, is forced by the momentum sink, which transports the particles. A detailed derivation of the back coupling mechanism in the numerical framework is described in Chapter 4. This sketch only serves as a simplified, conceptual image. However, the amount of additional complexity is plentiful. A brief literature summary is provided in the following to show the complexity of the turbulence modulation effects caused by particles/droplets.

2.3 Turbulent modulation

As seen in Fig. 2.9, the turbulence modulation can lead to a damping of the gas phase velocity variance. However, the interaction can also cause enhancement of the overall turbulence. This is demonstrated in Fig. 2.10 using the simplified model problem again. Here, g in Eq. 2.20 is unequal zero and adds momentum to the particle phase. This couples back to extra momentum for the gas phase. The damping and enhancement effects are discussed further in a short literature summary.

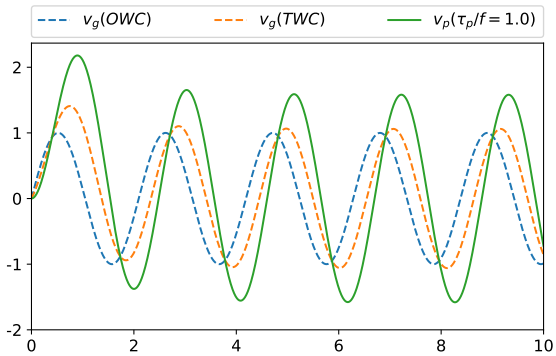

Figure 2.10: *Influence of the two-way coupling mechanism on the gas velocity. Same case as in Fig.2.9 but with an extra momentum source for the particles.*

Hetsroni [29] assumed based on theoretical considerations and experimental data (e.g. [30–33]) that the main parameter governing turbulence modulation is the particle Reynolds number Re_p (Eq. 2.19). He focused here on the global TKE level and sees the reason for the enhancement of turbulence caused by wake shedding. However, this conclusion counts only for flows, where the wake behind particles is the dominant TKE production mechanisms. Nonetheless, many flow configurations gain turbulence from several different mechanisms, which are not as easy to differentiate. Squires & Eaton [34] followed by Boivin et al. [35] investigated particle-laden homogeneous isotropic turbulence (HIT) using direct numerical simulation (DNS) and showed an overall attenuation of the turbulent kinetic energy (TKE) and of the energy dissipation rate, both induced by the momentum exchange with the particle phase. This agrees with Hetsroni's findings, because Re_p was very low in this case. However, for smaller scales of the TKE spectrum, an enhancement of TKE is observed.

Ferrante et al. [36] studied with DNS particle-laden decaying HIT, which leads to an slightly higher Re_p as the studies carried out earlier. They separated the droplet sizes into three regimes based on St (see Eq. 2.25 and Fig. 2.11): microparticles ($St < 1$), critical particles ($St \sim 1$) and large particles ($St > 1$), and described their effect as follows. Microparticles enhance the TKE and the viscous dissipation rate with respect to

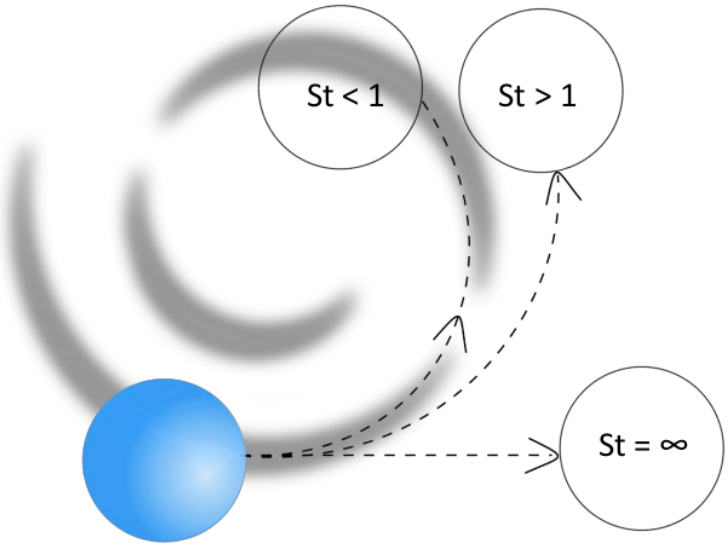

Figure 2.11: *Sketch displaying the behavior of particles with different St.*

the unladen case by remaining in their surrounding vortices due to their short response time and adding inertia to them. This results in a slower decay of HIT. A different modulation characteristic can be seen with large particles: due to their high momentum their trajectories cross vortices, which produces extra turbulent structures. This results in a faster decay of TKE and strain rate. The critical particles are a special case because of their accumulating characteristics in low vorticity regions. Thus, the turbulent scales are nearly not affected by their existence. Strain rate and dissipation rate are nearly equal to the single phase flow. As decaying HIT is a very feasible experimental test case, many other studies using DNS [37–40] and experiments [41, 42] followed and showed similar trends.

As mentioned previously, additional levels of complexity are endless. In this thesis we focus on the most commonly investigated parameters Re_p, St and the mass loading ϕ, which defines the ratio of particle to gas phase mass.

2.4 Parameter ranges in target region

The initial motivation for the topic of this thesis are fuel sprays in engines. Therefore, it is relevant to show that the assumptions and parameter ranges of the approach followed here are indeed encountered in a typical engine configuration. Therefore, we used the results of an LES spray simulation, studied by Giovanni Tretola at Imperial College using the LES code described in the appendix, to test the assumptions. The chosen test case for the evaluation will be a turbulent liquid jet issuing into stagnant air, known as Spray G from

Table 2.1: Major physical parameter of the flow configuration of Spray G from ECN.

ρ_l/ρ_g	μ_l/μ_g	d_l [μm]	Re_l	We_l
180	0.04	100	14500	72500

the Engine Combustion Network (ECN). A summary of the major physical parameters of the configuration of the test case is shown in Table 2.1. The Σ-PDF method has been implemented in Open-FOAM using a finite volume formulation. This implementation and its capabilities for turbulent multi–phase flows are presented in [43].
As described before the two-way coupling approach is valid until a volume loading of 10^{-2} (see Chapter 2.2.3), which gives in this configuration a mass loading ϕ of nearly 2. The other limit, in which no turbulence modulation is expected, is for a volume loading below 10^{-5}, which corresponds with a mass loading of 10^{-3}. Both limits are displayed in Fig. 2.12 with a black line for $\phi = 2$ (except in Fig. 2.12a, where it represents $\phi = 10$) and a white line for $\phi = 10^{-3}$. Fig. 2.12 depicts the results at a single time step and just serves as an estimate of the parameter ranges.

Fig. 2.12a shows the target region in which we assume the most significant impact of an SGS model for turbulent modulation effects caused by small droplets. To determine the parameter range of St and Re_λ for the studies Figs. 2.12b and 2.12c show their values in the region in which $10^{-3} < \phi < 2$. The range of St for the droplets are in between 0.5 and 10. Re_λ has a range between 30 and 400. These ranges serve as an orientation for the future studies to investigate the physical mechanism in these regimes. In this thesis, the different approaches of multiphase LES will not be discussed in details, but a short description of how an SGS model based on the ODT work in this thesis could look like is presented in the appendix.

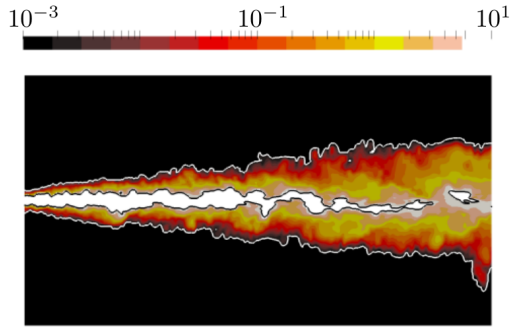

(a) ϕ

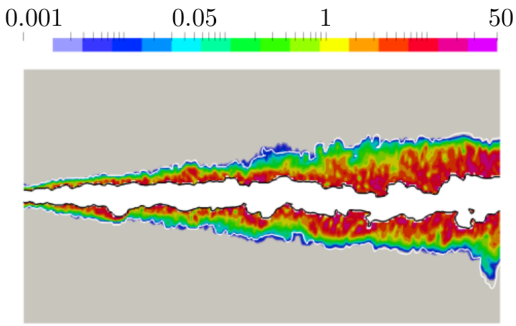

(b) St

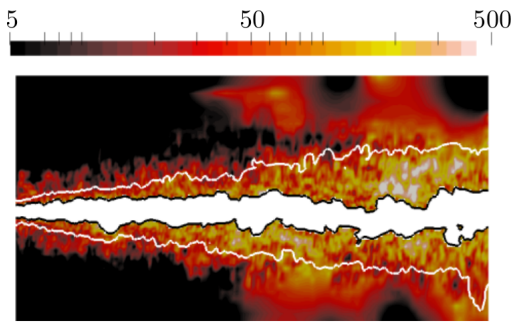

(c) Re_λ

Figure 2.12: *Contour plots of ϕ (a), St (b), and Re_λ (c) of a spray LES simulation by Tretola. White line: $\phi = 10^{-3}$, black line: $\phi = 2$ (Except in (a), where it is $\phi = 10$).*

3 One-Dimensional-Turbulence

This section describes the concept of the general ODT model in a temporal-planar description as used in Paper C, E and F, which form the main scientific contribution of this thesis. Remarks are added to the spatial-cylindrical formulation used in Paper A and B but for details the reader is referred to Paper F.

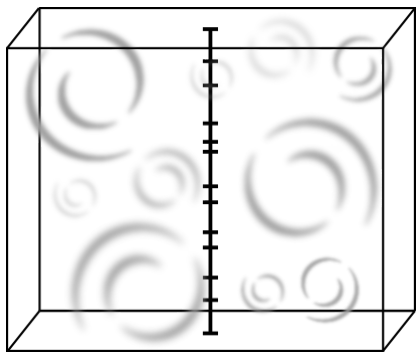

Figure 3.1: *Schematic representation of the ODT line as a line of sights.*

ODT is a stochastic model to simulate turbulent flows on a one-dimensional domain that is usually oriented in the direction of the largest mean velocity gradient, where the dominant turbulence effects are expected. The ODT line domain can be interpreted as a line of sight through a 3D flow field (Fig. 3.1). ODT is a numerical method to simulate individual realizations of turbulent flows. The main results of any ODT simulation are statistical quantities evaluated from running numerous single realizations or over a sufficiently long time interval.

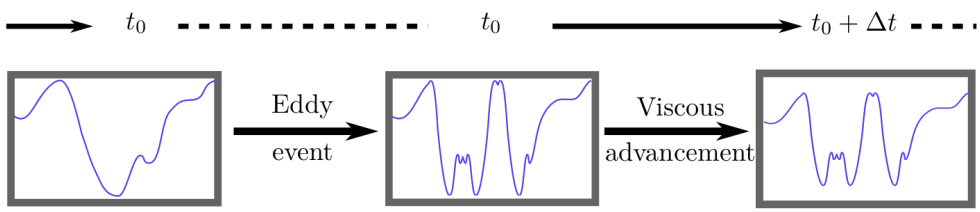

Figure 3.2: *ODT procedure on a random velocity profile. First, an eddy event is implemented at time t_0 instantaneous and, subsequently, the profile is advanced for a time increment Δt.*

In ODT, time advancement consists of viscous transport and a stochastic model to mimic turbulence effects on the profile for all variables along a one-dimensional line. Due to the one-dimensional setup there is no advective transport via a mean velocity in the direction of the ODT line and all advective transport is deemed to be turbulent via so-called *eddy*

events, see below. As a consequence, there is no pressure gradient present in the ODT governing equations as this is, as mentioned before,related to the acceleration of the mean flow. The full range of scales in time and space of the turbulent cascade are resolved. The latter consists of eddy events, in which the fluid property profile is rearranged by implementing triplet maps, defined below, in a manner consistent with turbulence scaling laws, followed by momentum changes within the individual fluid parcels comprising the eddy. The latter step represents pressure-fluctuation effects. Time advancement of viscous transport is paused at the times of occurrence of eddy events to allow eddy implementation, which is instantaneous, before viscous advancement resumes. This procedure is visualized in Fig. 3.2.

3.1 Viscous advancement

Deriving the governing equations of an arbitrary quantity ϕ for a control volume with fixed boundaries over time dt (seen in Fig. 3.3), we start with the Reynolds transport theorem (RTT):

$$\frac{d}{dt}\int\limits_{\Omega}\rho\phi\ dV = \underbrace{\frac{\partial}{\partial t}\int\limits_{\Omega}\rho\phi\ dV}_{\text{changes inside}} + \underbrace{\int\limits_{\partial\Omega}\rho\phi(\vec{u}\cdot n)\ dS}_{\text{fluxes through the boundaries}} \quad , \tag{3.1}$$

where Ω is the control volume and $\partial\Omega$ its boundary surface. The difference between normal velocity of the boundary and the flow velocity is represented by $\vec{u}\cdot n$.
Before deriving the governing equations for mass and momentum it is important to determine the control volume and its boundary surface on a planar ODT line.

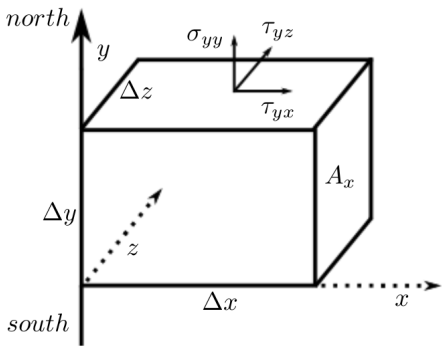

Figure 3.3: *Sketch of rectangular control volume Ω. e_i is a unit vector of the i-th direction.*

The volume of a rectangular control segment Ω with the edges Δx, Δy, and Δz is defined as $|\Omega| = V = \Delta x\Delta y\Delta z$. Its boundary surface is given by the two ODT line-normal surfaces north n and south s. The area of the surfaces is equal to the cross-section of the cell and given by $A_c = \Delta x\Delta z$. To preserve the dimensionality of mass and momentum on

the one-dimensional domain the cell volume is defined as the product of a cell cross-section area A_c and the cell length Δy on the ODT line, i.e. $V = A_c \Delta y$. This determination can be arbitrary, but will be important when treating extensive quantities, e.g. finite particle numbers.

The governing equations for mass and momentum are based on the Reynolds transport theorem in incompressible form and result in the continuity and momentum transport equations, respectively. All advection in the regarded cases is deemed to be turbulent and therefore is represented by the eddy events, so the advancement equations below do not include advective terms.

The mass balance equation follows the RTT (Eq. 3.1) with $\phi = 1$:

$$\frac{d}{dt}\int\limits_{\Omega} \rho \; dV = \frac{\partial}{\partial t}\int\limits_{\Omega} \rho \; dV + \int\limits_{\partial\Omega} \rho(\vec{u}\cdot n) \; dS. \tag{3.2}$$

As no mass source terms are considered in the control volume Ω during time increment dt, and no mass flux is allowed due to the incompressibility assumption, the right hand side is zero and the general mass balance is given as

$$\frac{d}{dt}\int\limits_{\Omega} \rho \; dV = 0. \tag{3.3}$$

For a given grid cell and assuming $\phi = const$ this leads to

$$\frac{d}{dt}\rho V_c = 0. \tag{3.4}$$

For the momentum balance Eq. 3.1 is used with $\phi = u_i$, where u_i represents the i-th velocity component.

$$\frac{d}{dt}\int\limits_{\Omega} \rho\phi \; dV = \frac{\partial}{\partial t}\int\limits_{\Omega} \rho u_i \; dV + \int\limits_{\partial\Omega} \rho u_i(\vec{u}\cdot n) \; dS. \tag{3.5}$$

Considering that no momentum is lost or gained inside the control volume during a time increment dt the first right hand side term is zero. Across the boundaries we consider three contributions to the momentum flux. These three are the viscous stresses τ_{ij} acting on the control volume, the contribution of turbulent advection, $d_{\rho u_i}$, and the momentum transfer between dispersed and gas phase $S_{p,i}$. $d_{\rho u_i}$ is completely governed by eddy events, which are presented in Chapter 3.2.

As the pressure gradient is neglected in the flow configurations considered, the momentum balance equation is given as

$$\frac{d}{dt}\int\limits_{\Omega} \rho u_i \; dV = \int\limits_{\partial\Omega} \tau_{ij} \; dS + d_{\rho u_i} + S_{p,i}, \tag{3.6}$$

where $\tau_{ij} = \mu \left(\frac{\partial u_i}{\partial x_j} + \frac{\partial u_j}{\partial x_i} \right)$ is the three-dimensional stress tensor. In the one-dimensional setup of the ODT framework only gradients in ODT line direction are resolved and therefore the stress tensor has only three non-vanishing components

$$\tau_{yx} = \mu \frac{\partial u_x}{\partial y}, \qquad \tau_{yy} = \sigma_{yy} = 2\mu \frac{\partial u_y}{\partial y}, \qquad \tau_{yz} = \mu \frac{\partial u_z}{\partial y}. \tag{3.7}$$

By rearranging and integrating over the cell volume and surfaces the momentum balance for a given grid cell is defined as

$$\frac{du_i}{dt} = \frac{1}{\rho V_c} \left(\tau_{yi,s} A_s - \tau_{yi,n} A_n + d_{\rho u_i} + S_{p,i} \right). \tag{3.8}$$

Eq. 3.8 is the equation which governs the diffusion and non-advective advancement, i.e. momentum exchange between phases, of the ODT line. The governing equations for the spatial-cylindrical framework are derived in the same manner, and are in detail described in [44] and [45].

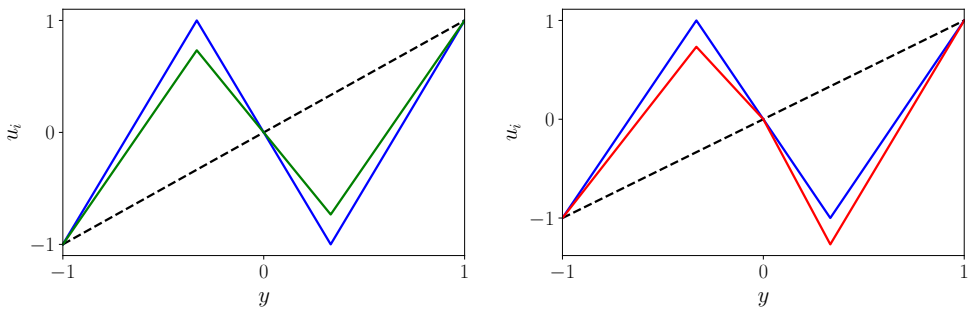

Figure 3.4: *Illustration of eddy events applied to a linear velocity profile, where the events involve three different choices of kernel coefficients. (− −) original profile of a given velocity component u_i, (—, blue) profile after eddy event without kernel ($c_i = 0$, $b_i = 0$), (—, green) profile after eddy event with kernel coefficient $c_i \neq 0$, $b_i = 0$ (a) and (—, red) profile after eddy event with kernel coefficient $b_i \neq 0$, $c_i = 0$ (b).*

3.2 Eddy events

For modelling turbulent advection on a 1D domain, Kerstein [7] introduced eddy events to capture each eddy as an instantaneous event, which cannot interact directly with other eddies. This event contains geometrical modifications of the velocity and scalar profiles exclusively in a selected interval $y_0 < y < y_0 + l$. l, the eddy size, and y_0, the eddy position, are randomly sampled numbers between fixed intervals of a set length range or

a position over the domain, respectively. The modification follows the surjective mapping rule called *triplet map* known from the Linear-Eddy-Model (LEM) [46] . In $[y_0, y_0 + l]$, a fluid at location $f(y)$ is being mapped to location y, where $f(y)$ is given as

$$f(y) = y_0 + \begin{cases} 3(y - y_0) & \text{if } y_0 \leq y \leq y_0 + \frac{1}{3}l \\ 2l - 3(y - y_0) & \text{if } y_0 + \frac{1}{3}l \leq y \leq y_0 + \frac{2}{3}l \\ 3(y - y_0) - 2l & \text{if } y_0 + \frac{2}{3}l \leq y \leq y_0 + l \\ y - y_0 & \text{otherwise.} \end{cases} \tag{3.9}$$

Comparing Bradshaws profile (Fig. 2.2) of the stretching process with the fluctuation profile after the triplet map (Fig. 3.4), we can see obvious geometrical similarities. This map reflects the compressive and rotational attributes of eddy motion. Its character increases the strain intensity and decreases the strain length scale. Although the mapping process itself preserves momentum and energy of the velocity profile, it adds velocity variance and, thus, turbulent kinetic energy, as seen in Fig. 3.4.

According to Kolmogorov's first hypothesis and the pressure-scrambling phenomena (see Chapter 2.1), an essential feature of turbulence is the phenomenon of return-to-isotropy for the small turbulent motions, which requires on the ODT modeling side a redistribution of TKE among the velocity components. Additionally, momentum and energy exchange between phases (as in the present application) and between kinetic and gravitational potential energy (as in buoyant stratified flow applications) has to be ensured. This is achieved by introducing a kernel transformation that follows the mapping operation. The complete eddy event is denoted symbolically as

$$u_i(y) \rightarrow u_i^{\mathrm{TM}}(y) + c_i K(y) + b_i J(y), \tag{3.10}$$

where u_i is the velocity in the i-th direction before and u_i^{TM} is the velocity after the mapping process. The kernel $K(y)$ is defined as the fluid displacement profile $y - f(y)$ that is induced by the triplet map and integrates to zero over the eddy region, so, for constant density, it does not induce an overall momentum change. $J(y)$ is the absolute value of $K(y)$ and so it does not integrate to zero over the eddy region (Fig. 3.5). Thus, it forces momentum change of the profiles if its coefficient b_i is non-zero. c_i scales the amplitude of $K(y)$. The effect of kernels on a linear velocity profile is illustrated in Fig. 3.4, indicating that the eddy-integrated momentum is modified by the J kernel but not by the K kernel.

Momentum conservation requires that

$$\rho \int_{V_e} \left(u_i^{\mathrm{TM}} + c_i K + b_i J \right) \, dV = \rho \int_{V_e} u_i \, dV - S_i. \tag{3.11}$$

V_e is the volume of the eddy region on the ODT line. S_i represents the sum of component-i inter-phase momentum penalties over the particles within the eddy volume. The evaluation of S_i is explained in Chapter 4. The triplet map conserves momentum, so by definition $\rho \int_{V_e} u_i \, dV = \rho \int_{V_e} u_i^{\mathrm{TM}} \, dV$, and with $\rho \int_{V_e} c_i K \, dV = 0$. Eq. 3.11 can be solved for b_i as

$$b_i = \frac{-S_i}{\rho \int_{V_e} J \, dV} \equiv M_i. \tag{3.12}$$

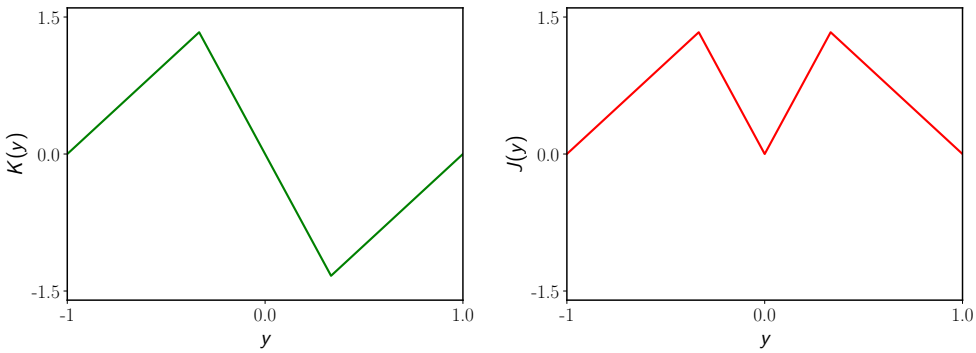

(a) (b)

Figure 3.5: *Illustration of kernel function $K(y)$ (a) and $J(y)$ (b).*

Similarly, the energy balance is used to evaluate c_i. The map-induced change of the domain-integrated kinetic energy of velocity component i is

$$\Delta E_i = \frac{\rho}{2} \int_{V_e} (u_i^{\mathrm{TM}} + c_i K + b_i J)^2 \, dV - \frac{\rho}{2} \int_{V_e} u_i^2 \, dV, \tag{3.13}$$

where ΔE_i includes any sink and source terms, which in this study are the energy transfers $S_{E,i}$ from the particle phase. Due to energy conservation during triplet mapping, $\int_{V_e} u_i^2 \, dV = \int_{V_e} (u_i^{\mathrm{TM}})^2 \, dV$ and it follows that

$$\begin{aligned} \Delta E_i = \frac{\rho}{2} \int_{V_e} (&2 c_i u_i^{\mathrm{TM}} K + 2 b_i u_i^{\mathrm{TM}} J \\ &+ 2 c_i b_i K J + c_i^2 K^2 + b_i^2 J^2) \, dV. \end{aligned} \tag{3.14}$$

Reordering in powers of c_i and inserting Eq. 3.12 for b_i yields

$$\begin{aligned} \Delta E_i = c_i^2 \underbrace{\frac{\rho}{2} \int_{V_e} K^2 \, dV}_{S} \\ + c_i \underbrace{\rho \left(\int_{V_e} u_i^{\mathrm{TM}} K \, dV + M_i \int_{V_e} K J \, dV \right)}_{P_i} \\ + \underbrace{M_i \rho \left(\int_{V_e} u_i^{\mathrm{TM}} J \, dV + \frac{M_i}{2} \int_{V_e} J^2 \, dV \right)}_{T_i}. \end{aligned} \tag{3.15}$$

For clarity, Eq. 3.15 is expressed in a shorter form as

$$\Delta E_i = c_i^2 S + c_i P_i + T_i. \tag{3.16}$$

The solution for c_i is

$$c_i = \frac{1}{2 \cdot S} \left(-P_i + \text{sign}(P_i) \sqrt{P_i^2 - 4S(T_i - \Delta E_i)} \right). \tag{3.17}$$

The choice of solution branch ensures that $c_i \to 0$ as $4S(T_i - \Delta E_i) \to 0$ [47]. ΔE_i specifies the re-distribution of the component energies. For this re-distribution, it is useful to evaluate the maximal energy Q_i that is available to subtract. This is determined by maximizing the right-hand side of Eq. 3.16 with respect to c_i, giving

$$-\Delta E_i|_{\max} = Q_i = \frac{P_i^2}{4S} - T_i. \tag{3.18}$$

Given the maximal available energy change, Q_i, the energy distribution towards each component differs for the test cases of HIT and HST.

For HIT, we aim for an isotropic re-distribution and the energy change for a given component is computed as

$$\Delta E_i = \alpha \left[\frac{Q_j}{2} + \frac{Q_k}{2} - Q_i \right] - S_{E,i}. \tag{3.19}$$

$S_{E,i}$ represents the sum of inter-phase energy exchange. α is an additional model parameter with its allowed range $0 \leq \alpha \leq 1$. In HIT α is chosen to be $2/3$ in accordance with a previously explained physical interpretation [47].

Regarding experimental [48] and DNS [49] data of HST, summarized in Pope [12], the re-distribution has an anisotropic characteristic. Thus, in HST only two components are chosen randomly which exchange energy. This makes three different combinations ij possible and this therefore called *three-eddy-type model*. The probability of each eddy event type is determined as follow,

$$p_{xy} = p_{xz} = (1 - p_{yz})/2, \tag{3.20}$$

where p_{yz} is chosen to be 0.2 to capture the TKE proportions mentioned in Rogers and Moin [49].

Given the maximal available energy change, Q_i, the energy change for a given component is computed as

$$\Delta E_i = \alpha \big[Q_j - Q_i \big] - S_{E,i}. \tag{3.21}$$

α is chosen to be 1, similar to Ashurst & Kerstein [50]. A parameter study is shown in Tab. 3.1 .

3.3 Eddy event rate

As a next step, it is important to define the eddy event rate distribution $\lambda_e(l)$, where $\lambda_e(l)\ dl$ is the frequency of the events in the size range $[l, l + dl]$ per unit length along the

Table 3.1: Parameter study of α and p_{yz} on TKE budgets in HST, compared to DNS data [49].

	α	p_{yz}	u'^2/k	v'^2/k	w'^2/k
ODT	1.0	0.2	1.05	0.343	0.6
	0.5	0.33	1.5	0.24	0.23
	0.5	0.2	1.5	0.18	0.3
DNS	–	–	1.06	0.32	0.62

y-coordinate. This is parameterized by the eddy origin y_0 and length l, and depends on the current flow state within that interval [7]. Based on this definition, $\lambda_e(l)$ has units (length^2·time)$^{-1}$ and is given as

$$\lambda_e(t; y_0, l) = \frac{C}{\tau_e(y_0, l) l^2}. \tag{3.22}$$

C is an adjustable eddy rate parameter and scales the overall eddy event frequency. To determine the eddy timescale τ_e we use the available kinetic energy in the sampled size-l region. Based on the scaling assumption for kinetic energy $E_{kin} \sim \frac{1}{2} m v^2 \sim \frac{1}{2} \rho V_e \frac{l^2}{\tau_e^2}$, the eddy time scale is modeled as

$$\frac{1}{\tau_e} = \sqrt{\frac{2}{\rho V_e l^2}(E_{\text{kin}} - Z E_{\text{vp}})}, \tag{3.23}$$

where $E_{kin} = \frac{KK}{V_e l^2} \sum_i Q_i$, V_e is the volume of the sampled eddy region and $KK = \int_{V_e} K^2 \, dV$. Q_i is the available energy defined in Eq. 3.21. In the three-type-eddy model the sum over i contains only the involved components sampled through Eq. 3.20. This reflects the total available TKE in the eddy region. An additional term, E_{vp}, is subtracted to reflect viscous dissipation effects and suppresses smaller eddies as physically possible. The viscous penalty energy is given as $E_{\text{vp}} = \frac{V_e}{2l^2} \frac{\mu^2}{\rho}$ and ρ and μ are eddy volume averages of density and dynamic viscosity, respectively. They are assumed to be constant in the studied cases. Z is the viscous penalty parameter and tuned to suppresses non-physical small eddies.

The integral of λ_e over y_0 and l defines the rate Λ_e of all eddies. Then the instantaneous joint probability density function (PDF) of eddy size and location is given as

$$P(y_0, l) = \frac{\lambda_e(y_0, l)}{\int\int \lambda_e(y_0, l) \, dy_0 \, dl} = \frac{\lambda_e(y_0, l)}{\Lambda_e}. \tag{3.24}$$

We assume that the occurrence of eddies follows a Poisson process in time with a mean rate Λ_e, i.e.

$$P(\Delta t) = \Lambda_e \exp(-\Lambda_e \Delta t). \tag{3.25}$$

Here, P denotes the PDF of the time between successive occurrences.

Computing Λ_e newly at each state of the flow requires complete integration and to sample from Eqs. 3.24 and 3.25 they have to be inverted. This procedure is computationally prohibitive. Here, a cheaper method is used based on the *thinning procedure*. As a first step, a time increment Δt is sampled with a mean rate $\hat{\Lambda}_e$, which needs to be greater than Λ_e. This rate is initially set high and decreases as desired during the computation. Secondly, the eddy origin y_0 and length l are randomly sampled from the probability distribution

$$\hat{P}(y_0, l) = \frac{\hat{\lambda}(y_0, l)}{\hat{\Lambda}}. \tag{3.26}$$

This PDF is modeled as $\hat{P}(y_0, l) = f(l) \cdot g(y_0)$, where $g(y_0)$ is uniform over the domain while the eddy size distribution is assumed to be

$$f(l) = A_l e^{-2\tilde{l}/l}. \tag{3.27}$$

A_l is the PDF normalization constant and $\tilde{l}$ is the most probable eddy size [51]. The form of $f(l)$ does not influence the spectrum, but the efficiency of the method.

Using Eq. 3.26, rearranged with regard to $\hat{\lambda}(y_0, l)$, the eddy acceptance probability $Pa = \frac{\lambda(y_0,l)}{\hat{\lambda}(y_0,l)}$ is reformulated as

$$Pa = \frac{\lambda(y_0, l)}{\hat{\Lambda}\hat{P}(y_0, l)}. \tag{3.28}$$

$\hat{\Lambda}$ is set such that Pa never exceeds unity. Now, a random number r in the interval $[0 < r < 1]$ is sampled and if r is smaller than Pa the eddy is accepted and will be implemented. Independent from accepting en eddy or not the time will be advanced for Δt by using the viscous transport and subsequently a new random state (y_0, l) will be sampled again.

The eddy event sampling and implementation followed by the viscous transport ensure the turbulent cascade behavior from the inertial range to the viscous range in the ODT framework (see Chapter 2.1).

3.4 Kernel events

In HST the production of TKE is driven by the mean flow, which triggers the integral length scale eddies. These scales are either provided by the initial profile, in e.g. transient applications like jet flows, or are required to be forced into the system, like in stationary HIT. One forcing scheme method used in Paper E is described in this section.

In Fig. 3.5a the kernel function $K = y - f(y)$ is depicted and it can be seen that its implementation can subtract and add TKE. The amount and sign are controlled by the coefficient c_i. Using this kernel function without the triplet map enables us to inject TKE instantaneously, see blue curve in Fig. 3.6. The red curve demonstrates the evolution of the profile after 30 kernel events, 60 eddy events and the diffusion steps in between.

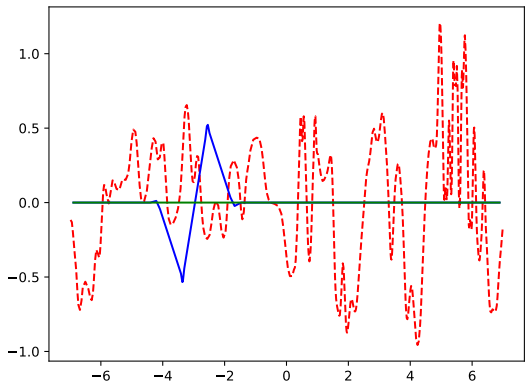

Figure 3.6: *The effect of kernel events on the initial profile (-,green). After one kernel event (-,blue). After 30 kernel and 60 eddy events (–,red), including diffusive advancement.*

The strategy for simulating stationary forced HIT is to keep the TKE constant in the system by performing an average of one external injection of TKE ΔTKE per time interval $1/\lambda_{ke}$. λ_{ke} is the mean occurrence rate of the TKE injection. Each injection, termed a kernel event, implements a kernel function similar to the one used during eddy events described above. It is specified to supply the needed TKE increment ΔTKE, which is determined below.

Based on a fixed domain length D and a fixed length l of the kernel event, chosen to match the integral length scale in the spectrum, the time interval $1/\lambda_{ke}$ is specified as

$$\frac{1}{\lambda_{ke}} = \frac{l}{D}T, \tag{3.29}$$

where T is chosen to be the large-eddy turnover time T_11 defined in Eq. 2.14. This assures that a given location experiences TKE injection once on average per large-eddy turnover time, consistent with the phenomenology of large-scale forcing. This phenomenology is governed by the dimensional expression for the production rate $\mathcal{P}$,

$$\mathcal{P} = C_{ke}\frac{l^2}{T^3}. \tag{3.30}$$

The production rate value $\mathcal{P}$, the length l, and time scale T of the forcing are required as inputs akin to the DNS forcing schemes of Eswaran & Pope [52]. Thus, C_{ke} is uniquely defined. Using Eq. 3.29 and 3.30 the interval can be written as

$$\frac{1}{\lambda_{ke}} = \frac{l^{5/3}}{D\mathcal{P}^{1/3}}C_{ke}^{1/3}. \tag{3.31}$$

The TKE increment ΔTKE that is required for the average rate of energy injection at any given location to match the energy production rate $\mathcal{P}$ is then

$$\Delta TKE = \frac{\mathcal{P}\rho D A_c}{\lambda_{ke}}, \tag{3.32}$$

where A_c is the cross-sectional area of each mesh cell as described before. Inserting Eq. 3.31 into Eq. 3.32 it follows that

$$\Delta TKE = \rho l^{5/3} P^{2/3} C_{ke}^{4/3} A_c. \tag{3.33}$$

Application of the kernel $K(y)$ within the event interval l can change the TKE in that interval by any desired amount without changing the total momentum in that interval, so this procedure is suitable for implementing the external TKE injection. Accordingly, the TKE injected by a kernel applied to the ith velocity component within the kernel-event volume V_k is specified as

$$\Delta TKE_i = \frac{1}{3}\Delta TKE = \frac{\rho}{2}\int_{V_k}[(u_i + d_i K(y))^2 - u_i^2]dV, \tag{3.34}$$

thus isotropically distributing the injected energy among onto the three velocity components. The component-i kernel coefficient d_i must be assigned so as to inject the specified TKE increment. However, the implementation of a kernel requires numerically to split cells over l and to define their displacement according to the triplet map function but without mapping the initial profile. Therefore, an interpolation of the profile to the new cell centers is required, which can causes small TKE variations. These variations can be captured by integrating before and after the cell splitting and interpolation procedure. Finally, they are added to ΔTKE_i and re-injected or subtracted. The term $\int_{V_k} K(y)^2 dV$ is analytically evaluated as $\frac{4}{27} l^3 A_c$ [50]. Solving Eq. 3.34 for d_i gives

$$d_i = \frac{27}{4 l^3 A_c}\left[- u_{i,k} + \sqrt{u_{i,k}^2 - \frac{8}{27\rho} l^3 A_c \Delta TKE}\right], \tag{3.35}$$

where $u_{i,K} = \rho \int_{V_k} u_i K dV$.

The occurrence times of kernel events are samples from a Poisson process (see Eq. 3.25). Therefore, as in Chapter 3.3 the sampled time intervals Δt_{ke} between randomly occurring, independent events with a mean rate of occurrence λ_{ke} are exponentially distributed. Due to the characteristics of forced HIT, the energy production rate P and dissipation rate ϵ are equal in absolute values averaged over time and in the following only mentioned as energy dissipation rate ϵ.

Concluding we can say that the three ranges in the TKE spectrum are modelled in ODT with three different methods. The production of TKE in the energy containing range is governed by eddy events working on the mean flow or a forced integral scale (e.g. kernel events). In the inertial subrange eddy events govern the cascade characteristics and decrease the scales until the viscous transport finally transforms it into thermal energy. This procedure is summarized in Fig. 3.7.

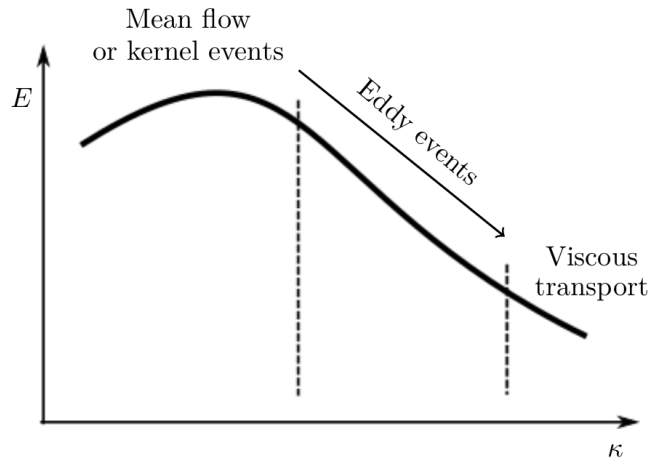

Figure 3.7: *ODT's turbulent cascade.*

4 Lagrangian particle model in ODT

In Chapter 2.2.2 we derived the governing equation, drag law (Eq. 2.23), for the evolution of a rigid, spherical particle using the point-source approach. Repeatingly, the main assumptions for the point-source approximation are that the particle size is small relative to the Kolmogorov length scale of the gas phase, the particle Reynolds number is low and the density ratio between gas and particle phase is high. The governing equations for each individual particle used in the following, here omitting gravity, are:

$$\begin{aligned} \frac{dv_{p,i}}{dt} &= -\frac{v_{p,i} - v_{g,i}}{\tau_p} f, \qquad && i = 1, 2, 3 \ , \\ \frac{dx_{p,i}}{dt} &= v_{p,i}, && i = 2 \ . \end{aligned} \tag{4.1}$$

$\tau_p = \frac{18\nu\rho_f}{d_p^2 \rho_p}$ and $f = (1 + 0.15 Re_p^{0.687})$, derived in Chapter 2.2.2 based on studies by Schiller and Naumann [27]. The subscripts p and g represent the particle and the gas phase, respectively. The coordinate $i = 2$ is aligned with the ODT coordinate direction y. Here, $v_{g,i}$ represents the undisturbed gas velocity. Using this equation, an obvious way to evolve an inertial particle is to incorporate the ODT-specified gas velocities $u_i(y,t)$ at a particle location y at time t. However, considering the previously introduced structure of the gas phase evolution, the particle evolution requires different treatment during the viscous transport and the eddy events. Furthermore, the particle is confined to the ODT domain and its spatial coordinate is $x_{p,2}$. The velocities v are accordingly termed eddy velocities. Where the component index i is omitted, the component $i = 2$ aligned with the ODT domain is implied, hence y_p is shorthand for $x_{p,2}$. ODT does not implement particle displacements in directions $i \neq 2$ because ODT captures only the domain-aligned displacements, which is sufficient for modeling representative behavior in isotropic and shear turbulence. All interpretation of the evolution in lateral and steamwise direction are not explicit within the model [1, 53]. Nevertheless, there is an intermediate step in the advancement process that requires evaluation of particle displacements $x_{p,i}$ in all coordinate directions i.

The drag law (Eq. 4.1) is solved by a first-order Euler method. Here, it is important to consider the limits of Eq. 4.1 using this method. In particular, if the time step exceeds the value of τ_p / f, the new particle velocity exceeds the gas velocity against the aim of the drag law to reach an equilibrium, which ends up to be unphysical.

4.1 Particle time advancement

Much as the gas phase treatment consists of time advancement of viscous transport punctuated by eddy events, the particle treatment consists of time advancement of the drag law, Eq. 4.1, punctuated by interaction of particles with the gas phase during the eddy events, which involves a different application of the drag law, as described in Chapter 4.2.

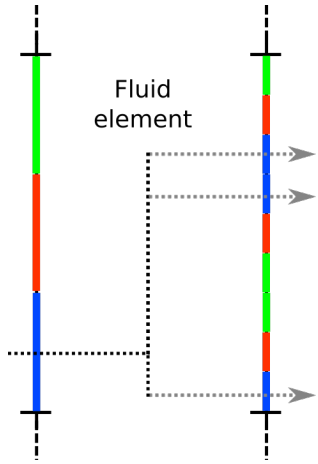

Figure 4.1: *Advection of a fluid element by triplet mapping.*

Particle advancement concurrent with viscous transport is described first.

One might suppose that the velocity components $v_{g,i}$ in Eq. 4.1 can be set equal to the ODT gas velocities u_i, but this is not the case because the advection of fluid elements occurs only by triplet mapping. Meaning during each time increment in the viscous advancement, they are fixed on the ODT line and only triplet mapping is allowed to reorder them (Fig. 4.1). One implication for particles is that, in the zero-inertia limit of vanishing τ_p, particles cannot deviate from the trajectory of the fluid elements that contain them (Fig. 2.11). During viscous transport, fluid elements are motionless in the ODT domain direction. Then zero-inertia particles must likewise be motionless. The only value of $v_{g,2}$ in Eq. 4.1 that is consistent with this requirement is zero. Considering the case of vanishing τ_p in Eq. 4.1, $v_{p,2}$ is forced to the value of $v_{g,2}$ and hence to zero. These results imply that there is no $i = 2$ contribution to the computation of Re_p for the time advancement.

In the other coordinate directions $i \neq 2$, $v_{g,i}$ is taken to be u_i for those components, where u_i is subject to viscous-transport advancement concurrently with particle time advancement. The particle trajectories in the $i \neq 2$-directions are not tracked due to the reduced dimensionality of the model and, thus, only their velocities are advanced.

Another limiting case that must be treated consistently is the infinite-inertia ballistic limit. Eq. 4.1 gives a zero-acceleration and so a constant-velocity motion in this limit for any time history of the gas velocity components, so the treatment of this limiting case is trivially correct. In contrast, the formulation of the particle-eddy interaction requires some care in order to enforce the correct behavior in this limit, as described in Chapter 4.2.

As particle momentum changes during the integration of Eq. 4.1, overall momentum conservation is maintained by distributing an equal and opposite momentum change uniformly to the gas within the mesh cell that contains it, thus implementing one of

the particle-gas two-way coupling mechanisms in the model. (The other is described in Chapter 4.2.) This feedback to the gas phase during particle time advancement is indicated by the particle contribution $S_{p,i}$ in Eq. 3.8 which is evaluated as

$$S_{p,i} = \sum_{N_c} m_p (v_{p,i} - v_{g,i}) \frac{f}{\tau_p}, \tag{4.2}$$

where N_c is the number of particles in the mesh cell (but particle and mesh cell indices are omitted in the summand for clarity).

4.2 Particle-eddy interaction

Due to the instantaneous character of eddy events, it is necessary to model the interaction between a particle and an eddy event, which we refer in the following to as particle-eddy interaction (PEI). Here, it is important to have in mind the distinction between physical vortex/eddy structures and eddy events in ODT. Schmidt et al. [1] developed the so-called instantaneous particle-eddy model (noted as *type-I*), which governs the domain-aligned displacement of particles due to an eddy event. This PEI model is used to capture particle-eddy interaction for each particle, which is located in the sampled eddy region. The main model assumption is that the eddy lifetime equals the eddy time scale τ_e (Eq. 3.23) multiplied by a coefficient β_p that is a model parameter. The PEI can persist no longer than the eddy lifetime but can be shorter in duration if the particle exits the volume occupied by the eddy (Fig. 4.2) before the PEI terminates at the end of the eddy lifetime. That means the integration of the motion of a particle in the ODT line direction based on Eq. 4.1 must take into account the time until a particle exits the region occupied by the eddy if that time is less than the eddy lifetime.

Before the latter point is addressed, the treatment of the drag law during the PEI is explained. It will be shown that modifications of the drag law are needed in order to satisfy consistency conditions. It is useful for this purpose to simplify the drag law by specifying that $v_{g,i}$ and τ_p/f are constant in time during the PEI. For $i \neq 2$, the constant value is chosen to be the value of u_i at the particle initial location y_{p0}. The specification of $v_{g,2}$ is explained shortly. The auxiliary variables $x_{p,i}$ for $i \neq 2$ are initialized to nominal values $x_{p0,i} = 0$.

On this basis, the analytical result of integrating the drag law over an arbitrary time interval t is

$$v_{p,i} = v_{g,i} - (v_{g,i} - v_{p0,i}) e^{-tf/\tau_p}, \qquad i = 1, 2, 3, \tag{4.3}$$

yielding the particle trajectory

$$x_{p,i} = x_{p0,i} + v_{g,i} t - \frac{\tau_p}{f} (v_{g,i} - v_{p0,i})(1 - e^{-tf/\tau_p}), \quad i = 1, 2, 3. \tag{4.4}$$

In Chapter 4.1, $v_{g,2}$ was set equal to zero in order to enforce consistency between particle and gas motion in the zero-inertia limit. The PEI likewise requires modification in this

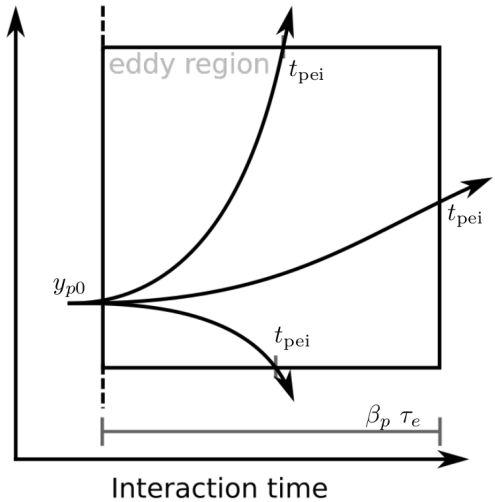

Figure 4.2: *Possible particle paths to exit the eddy region during the particle-eddy interaction (PEI).*

instance to enforce consistency in the infinite-inertia (ballistic) limit. As described in Chapter 2.3 and seen in Fig. 2.11, ballistic particles are not affected by turbulent eddies and should therefore experience no displacement during the PEI. However, the PEI advances particles during a time interval $t_{\mathrm{pei}} \leq \beta_p\ \tau_e$ starting at the instant of an eddy occurrence (Fig. 4.3). This advancement must be reversed to ensure the ballistic particle limit of the PEI.

The particle advancement for zero-inertia particles has no consequence due to this artifact because such particles are motionless during the advancement interval as a result of the consistency enforcement described in Chapter 4.1. All finite-inertia particles are subject to this artifact, but there is an exact remedy only for ballistic particles. As noted in Chapter 4.1, the advancement after eddy occurrence correctly produces the trajectory of a ballistic particle. The artifact can be avoided by modifying the drag law solution, Eqs. 4.3 and 4.4, so that its specialization to the ballistic limit produces no change in y_p or $v_{p,2}$ when the drag law is applied during the PEI. This gives the differences in position and velocity

$$\begin{aligned} \Delta y_p &= v_{g,2} t_{\mathrm{pei}} - v_{g,2} \frac{\tau_p}{f} (1 - e^{-t_{\mathrm{pei}} f/\tau_p}) \\ \Delta v_{p,2} &= v_{g,2} (1 - e^{-t_{\mathrm{pei}} f/\tau_p}). \end{aligned} \tag{4.5}$$

The corresponding post-PEI particle location and velocity are $y_p = y_{p0} + \Delta y_p$ and $v_{p,2} = v_{p0,2} + \Delta v_{p,2}$, respectively, where $v_{p0,2}$ appears in the latter equation because it has been zeroed out only in the expressions for the changes.

In the ballistic limit $\tau_p \to \infty$, Eq. 4.5 yields no change in y_p or $v_{p,2}$, as desired. Eq. 4.5 is

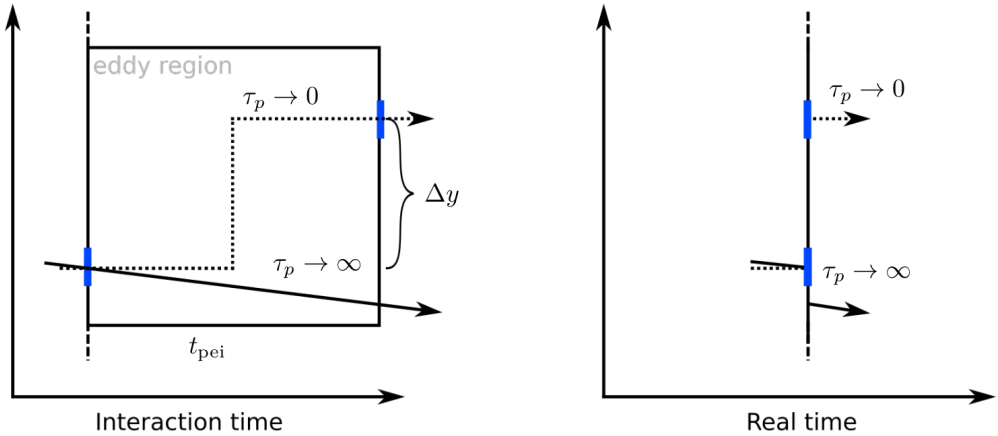

Figure 4.3: *Schematic diagram of the particle-eddy interactions in the interaction* t_{pei} *and real time coordinates for a ballistic* ($\tau_p \to \infty$) *and zero-inertia* ($\tau_p \to 0$) *particle. Additionally, it demonstrates the double counting of particle advancement. (Adapted from Schmidt [53].)*

likewise consistent with the zero-inertia limit, as explained below after the quantities $v_{g,2}$ and t_{pei} are defined.

For finite St, the modifications that yield Eq. 4.5 and the resulting expressions for y_p and $v_{p,2}$ do not constitute a physically consistent drag-law formulation. Nevertheless, this formulation smoothly interpolates between limits in which the formulation is physically correct. From this viewpoint the approximation is no more severe than idealizations inherent in the overall modeling framework.

Now, it is necessary to define the eddy velocity $v_{g,2}$ and to evaluate the interaction time t_{pei}. The determination of $v_{g,2}$ is based on the displacement of a massless (zero-inertia) particle by a triplet map as specified by Eq. 3.9. The triplet map provides three possible massless particle positions and a unique position is sampled randomly with a uniform distribution from those three possible ones. As illustrated in Fig. 4.1, triplet mapping of a massless particle identifies three possible particle displacements. A unique displacement is obtained by randomly choosing one of the displacements, all of which are equally probable. This procedure was previously presented as a model assumption with no statement of an underlying physical or mathematical basis [54]. The mathematical basis of this procedure is explained in Appendix A by Fistler et al. [55] (Paper E).

The chosen displacement Δy, see Fig. 4.3, divided by t_{pei} defines the eddy velocity $v_{g,2}$ during the PEI. Based on the zero-inertia limit of Eq. 4.5, this enforces the zero-inertia consistency condition.

As a next step the interaction time scale t_{pei} has to be determined and therefore a so-called

eddy box is introduced with the dimensions $[l \times l \times l]$, corresponding to the eddy interval l in ODT line direction and intervals $[-l/2, l/2]$ in each of the two coordinate directions normal to the ODT line direction. If the particle exits the eddy box through any face during the eddy lifetime, then the duration of the PEI is deemed to be the time until the exit of the box. Otherwise, it is the eddy lifetime (Fig. 4.2).

The eddy box reflects the consideration that the PEI can terminate either because the eddy motion has ended or because the particle leaves the volume containing the eddy before the end of the eddy motion. Although the model lives on the 1D domain, it evolves all three components of gas and particle velocity and therefore can evolve the particle trajectory in 3D under simplifying assumptions such as constancy of domain-normal gas velocity components in the domain-normal directions. The eddy box then defines the boundaries of the eddy region, allowing the particle exit time to be evaluated accordingly.

For directions $i \neq 2$, the time-to-exit (which need not exist because the particle could come to rest within the eddy box) is based on the direction-i trajectory given by Eq. 4.4. For $i = 2$ it is given by the expression given at the bottom line of Eq. 4.5, where the time argument in Eq. 4.4 is now the generic time variable t. The first crossing of any face of the eddy box determines the exit time.

$v_{g,2}$ is defined in terms of t_{pei}, but now there is the possibility that t_{pei} depends on $v_{g,2}$ because the exit time might be determined by the particle exiting the eddy box in the y direction. This possibility would exist if the drag law were implemented without modification. However, the initial particle velocity in direction $i = 2$ has been set equal to zero to obtain Eq. 4.5, which assures that the new particle position is in the range between initial particle position and the massless particle displacement for $St > 0$ and monotonically approaches the initial particle position as St increases (by construction, for consistency with the ballistic limit). Therefore particles cannot exit the eddy box in the y direction, so only directions $i \neq 2$ need to be checked. This is why it is possible to evaluate t_{pei} before evaluating $v_{g,2}$.

Eddy events displace particles and change their momentum in the domain-aligned direction. As in the treatment of particle time advancement in Chapter 4.1, this implies momentum exchange and thus energy exchange between the gas and particles within the eddy volume, implemented in this case as the final step of the eddy event. S_i and $S_{E,i}$ in Eqs. 3.11 and 3.21 respectively enforce gas momentum and energy changes that are equal and opposite to those of the particle phase, where

$$S_i = \sum_{N_\text{e}} m_p \Delta(v_{p,i}) \tag{4.6}$$

and

$$S_{E,i} = \frac{1}{2} \sum_{N_\text{e}} m_p \Delta(v_{p,i}^2). \tag{4.7}$$

These are summations over the N_e particles within the eddy volume, with the summation indices suppressed in the summands.

5 Highlights

In this chapter, the most significant outcomes of the thesis work are highlighted. The highlights are chronologically ordered.

Lagrangian Particle tracking in a spatial, cylindrical framework

As a first step, we carried out an investigation of the Lagrangian particle tracking method on a particle-laden jet test case (Paper A and B). This test case used a cylindrical representation of the flow field and was advanced spatially using the ODT method presented in Paper F. Sun et al. [11] studied this flow configuration before in a temporal, planar representation and transformed the temporal dimension into a spatial one. This transformation seemed to be error-prone and so the spatial formulation offered the chance to avoid this.

First, we evaluated the one-way-coupling mechanism by studying the statistics of the mean radial particle dispersion and the mean axial velocity of the particles. Therefore, we compared the ODT results with experimental data for different St and Re. Fig. 5.1 shows that the model predicts very well the dispersion of a particle with diameter $d_p = 90\mu m$ compared to the reference data. The model parameter β_p was tuned before to capture the mean radial dispersion for $d_p = 60\mu m$ accurately.

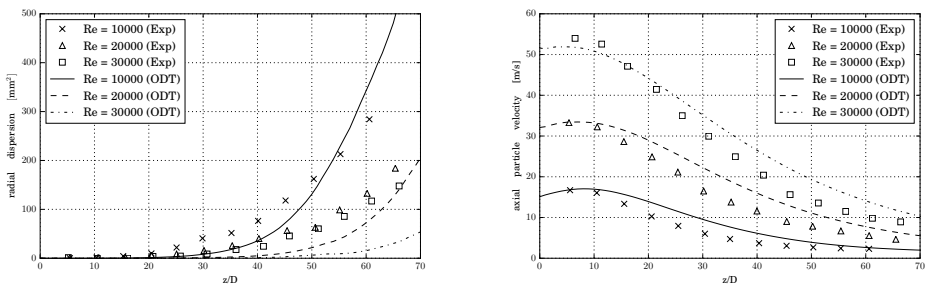

(a) *Mean radial dispersion of particles* (b) *Mean axial velocity of particles*

Figure 5.1: *Prediction of radial dispersion and axial velocity of particles with* $d_p = 90\mu m$

Secondly, a newly developed two-way coupling mechanism was studied as well for a particle-laden jet configuration and evaluated against experimental data by Budilarto [56]. This model could show its capabilities of predicting the axial mean velocity and its fluctuation on the centerline for different mass loading ϕ and d_p. Especially the data of the velocity fluctuation gives a first overview of the turbulence modulation effects caused by small particles on a jet, see Fig. 5.2. This flow configuration is very similar to the far

field region of a spray and the findings give a first impression of what to expect.

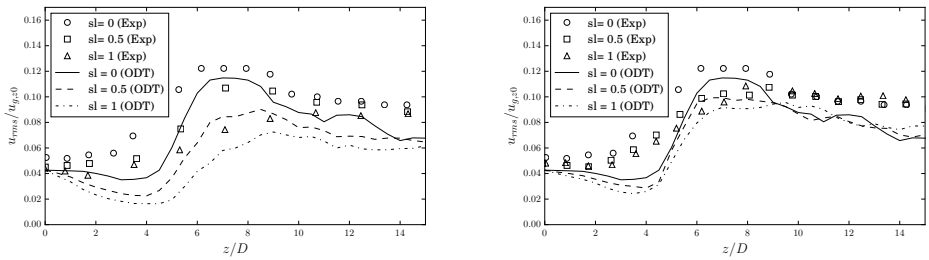

(a) $d_p = 25\mu m$ (b) $d_p = 70\mu m$

Figure 5.2: *Mean axial velocity fluctuation along centerline with different mass loading ϕ.*

Fig. 5.2a and 5.2b show that with increasing mass loading ϕ (here equal to sl for solid loading) the damping effect on the axial velocity fluctuation is increased as well. Additionally, it can be seen that the significants of this effect depends on the particle diameter. These findings give a first overview of the turbulence modulation effects caused by small droplets/particles.

Particle-laden homogeneous isotropic turbulence

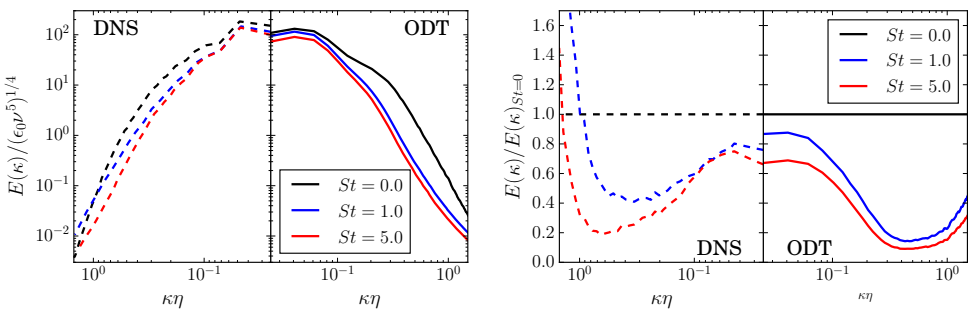

(a) (b)

Figure 5.3: *Dependence of the non-dimensionalized spectrum on Stokes number. $Re_\lambda = 70$ (DNS by Abdelsamie and Lee [57]).*

The next important step in this thesis work was the development of a forcing scheme in ODT to capture stationary, forced homogeneous isotropic turbulence (Paper D). It allowed us to validate the single-phase and particle-laden test cases against several sets of DNS results by Abdelsamie and Lee [57] and Boivin et al. [35]. The capability of ODT to capture the Kolmogorov spectrum of single-phase and particle-laden stationary HIT (Fig. 5.3) provides the opportunity to get detailed insights of the turbulence modulation

mechanisms despite its reduced dimensionality. Especially, the well-captured trend for different St in Fig. 5.3b shows the potential of ODT to contribute to a better understanding of parameter dependences on the turbulence modulation effect.

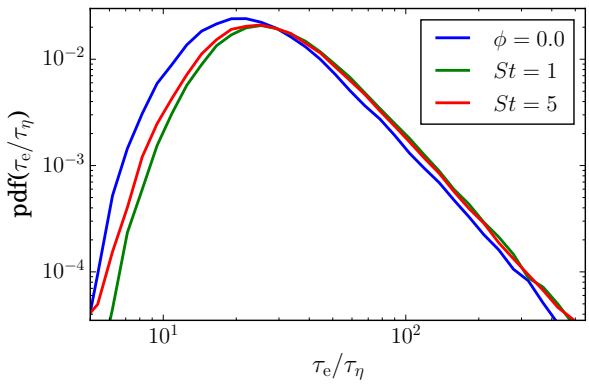

Figure 5.4: *Probability density function of the non-dimensionalized eddy time scale τ_e/τ_η, where τ_η for the unladen case is used, for different Stokes numbers for $\phi = 1.0$ (versus $\phi = 0.0$).*

Because ODT is a conceptual model containing two consecutive mechanisms, viscous advancement and eddy events, both can be separately evaluated and give details about them, which are challenging to distinguish in DNS. One example is the effect of particles on the probability density function for the eddy time scale τ_e (Eq.3.23). These data add a new perspective of the Stokes dependence on the particle-eddy interaction, still considering that eddy events are not exactly analogous to vortex structures in real flows. It showed that particles with St below unity should have the most influence on the pdf for fixed mass loading due to the increasing momentum and energy exchange during the PEI. Additionally, there is no particle-fluid interaction expected for $St = \infty$.

Additionally, we reported the complexity experienced for the ratio between TKE of the particle and gas phase k_p/k based on the choice of case parametrization. We consider k_p/k as a fundamental property of particle-laden turbulence, which has not been reported in other literature to the best of our knowledge, and it will require further validation by DNS or other means in the future. Overall the ODT results were very promising and enabled us to step forward to a new challenge of capturing particle-laden homogeneous shear turbulence.

Particle-laden homogeneous shear turbulence

The final ODT model extension of this thesis work was the development of the three-type-eddy model to capture turbulence statistics in anisotropic flows. This enabled us to investigate single-phase and particle-laden homogeneous shear turbulence (Paper E). The

detailed study on the single-phase, including agreements with transient and stationary DNS results, showed the strong capabilities of the developed method. Although, influences on the TKE spectrum of the particle-laden case (Fig. 5.5) were not as well captured as the previous results for HIT, the deviations could be explained in details and it did not discount the promising character to predict the global quantities k and ϵ. These two seem to be the most important quantities to predict for contributing to a new SGS model for LES.

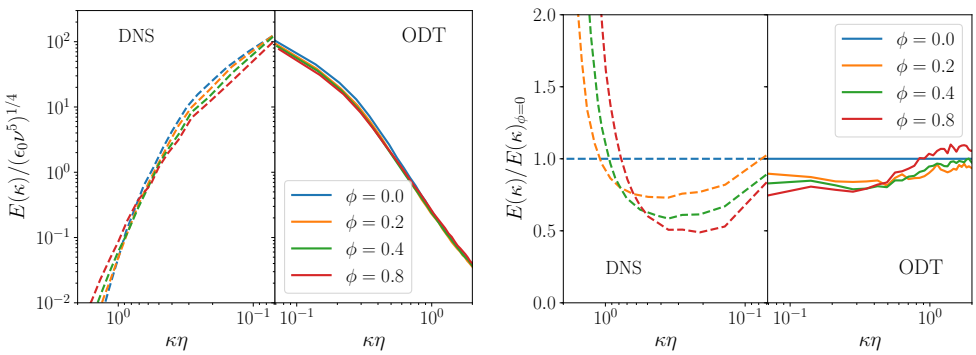

(a) (b)

Figure 5.5: *Dependence of the non-dimensionalized spectrum on mass loading.* $Re_\lambda = 43$, $St = 1$ *(DNS by Gualtieri et al. [58]).*

We could show that the ODT model reproduces qualitatively the parameter dependences of the global quantities k and ϵ that are not direction dependent, see Fig. 5.6. Despite the not sufficient capturing of the increase of turbulence anisotropy with increasing particle loading, its physically reasonable global parameter dependences suggest that it might provide useful guidance for the development of parameterized subgrid-scale (SGS) closure of large-eddy simulations (LES) of turbulence modulation by particles. Additionally, a consistently normalized comparison with ODT results for particle-laden HIT indicates significant differences between the two flows, but the broader picture is that the parameter dependences and other behaviors are analogous.

Eventually we were able to show that the three-eddy-type model, implemented to capture the anisotropic turbulence statistic, offers an additional degree of freedom to the energy redistribution. This extension also includes the option of isotropic coupling of velocity components, albeit two at a time, as a special case, so it is applicable to any flow to which ODT was originally formulated. Thus, the three-eddy-type model is recommended as a general-purpose alternative because it offers all capabilities than before and adds to them.

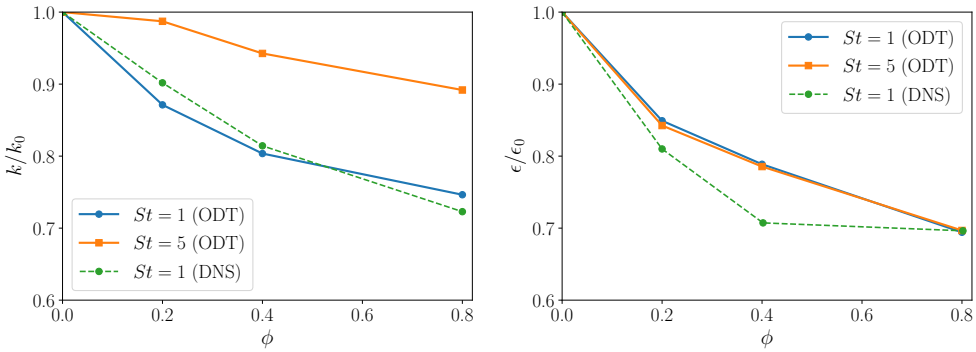

(a) k (b) ϵ

Figure 5.6: *Dependence of the fluid-phase TKE k (a) and rate of dissipation ϵ (b), normalized by the value for the single-phase case (k_0, ϵ_0), on mass loading for ODT. $Re_\lambda = 43$, (DNS by Gualtieri et al. [58]).*

Overview of model extensions

Extension	Test case	Investigations
Particle tracking in spatial, cylindrical coordinates	Particle-laden jet into stagnant air	Turbulence modulation effects caused by small particles in spray-like configuration
Forcing scheme to inject turbulent kinetic	Particle-laden homogeneous isotropic turbulence	Parameter dependences of turbulence modulation on Re_λ, St, and ϕ
Three-eddy-type model for flows with anisotropic turbulence statistics	Particle-laden homogenoeus shear turbulence	Parameter dependences of turbulence modulation and case-sensitivity between HIT and HST

6 Summary of Papers

Paper A

"Numerical study of stochastic particle dispersion using One-Dimensional-Turbulence"

The first required step for this thesis was to implement the particle model into the ODT 2.0 framework and modify it towards for the cylindrical coordinate system and an evolution in spatial dimension. Using the newly-developed spatial-cylindrical ODT promised an improvement of predicting the carrier gas-phase and a better comparison with spatial experimental results. In this paper the first validation of the new model was published. It is investigating the radial dispersion and axial velocity decay of a hexadecane droplets in a jet configuration with a nozzle diameter of 7 mm and Reynolds numbers ranging from 10000 to 30000. The ODT predicted data is compared with experiments of Kennedy and Moody [59] for a broad range of different Stokes numbers. The presented results show good agreement with the experimental data, reproducing the results of Sun et al. [11] without needing to transform the temporal coordinate.

Published in Proceedings of the ILASS-Americas 2017, Atlanta, USA (2017).

Division of work: The conceptual work was developed in collaboration with the co-authors. The implementation, simulation execution, and data post-processing were done by me. The paper was written together with all co-authors.

Paper B

"Numerical studies of turbulent particle-laden jets using spatial approach of one-dimensional turbulence"

As we successfully validated the particle tracking in the previous paper the next step was to extend the model for a momentum transfer from the particle back to the gas phase, i.e. a two-way coupling approach. Therefore, we introduced a source term for the diffusive advancement equation and a new kernel formulation enabling to exchange momentum and energy from and towards the particle phase. To validate this extension, simulations were run for a particle-laden turbulent round jet with mass loading $\phi = 0.0 - 1.0$ and particle diameter 25 μm and 70 μm and compared to experimental data from Budilarto [56]. It could be shown that the model was capable of capturing turbulence modulation of particles in a turbulent round jet.

Published in Proceedings of the ILASS-Europe 2017, Valencia, Spain (2017).

Division of work: The conceptual work was developed in collaboration with the co-authors. The implementation, simulation execution, and data post-processing were done by me. The paper was written together with all co-authors.

Paper C

"A new LES subgrid-scale approach for turbulence modulation by droplets"

This paper presents a conceptual description of how to use ODT to develop a SGS model for turbulence modulation by droplets. Due to the inexpensive computational costs of ODT the proposal presents a data gathering strategy of particle-laden HST flows for different parameters Re_λ, St and ϕ. It is proposed to use the Factorial design known from Design of Experiments. This study shows results for the original ODT framework capturing HST and could already show the promising potential of ODT for capturing turbulence modulation caused by particles/droplets.

Published in Proceedings of the ICLASS 2018, Chicago, USA (2018).

Division of work: The conceptual work was developed in collaboration with the co-authors. The implementation, simulation execution, and data post-processing were done by me. The paper was written together with all co-authors.

Paper D

"Turbulence modulation in particle-laden, stationary homogeneous isotropic turbulence using one-dimensional-turbulence"

The previous extension of ODT to particle-laden flows and then to two-way fluid-particle coupling is now used to study particle-laden stationary, forced HIT. Stationary HIT is considered a simple test case for the first step towards relevant data for SGS closure of LES. Therefore, a novel approach to large-scale forcing in ODT was developed. The single-phase and particle-laden test cases were validated against several sets of DNS results by Abdelsamie and Lee [57] and Boivin et al. [35]. ODT reproduces the spectral profile of turbulence modulation that is induced by the two-way coupling in DNS. An important feature of this modulation is the shift of spectral intensity from scales somewhat larger than the Kolmogorov microscale to scales in the vicinity of the Kolmogorov microscale. Owing to the transparent phenomenology implied by the model formulation, this behavior has been readily diagnosed. The dissipative nature of point-particle time advancement in DNS as well as ODT contributes to the high-wave-number upturn. This raises the question of the extent to which this behavior is physical rather than a numerical artifact of both methods.

The ODT model features enable physics investigation presently beyond the scope of DNS or any other existing methodology. The implemented forcing mechanism is non-dissipative for particle-laden as well as single-phase flow, so parameter studies are possible with ϵ held fixed while varying St and ϕ. Additionally, the low computational cost of ODT creates opportunities for extensive future parameter studies. Also, the study reports results for the ratio of particle-phase and fluid-phase TKE over a wide range of St and ϕ, which was not found in the literature before.

Published in Physical Review Fluids 5 (2020).

Division of work: The conceptual work was developed in collaboration with the co-authors. The implementation, simulation execution, and data post-processing were done by me. The paper was written together with all co-authors.

Paper E

"Turbulence modulation in particle-laden stationary homogeneous shear turbulence using one-dimensional turbulence"

The natural configuration of SGS turbulence in LES is homogeneous sheared turbulence (HST). With the original redistribution of energy in ODT during an eddy event it was not possible to capture anisotropic turbulence structures, which are dominant in HST. Therefore, ODT is modified with a novel approach of energy component coupling during eddy events. Each eddy event is assigned to only two components which exchange TKE. This gives one eddy types for each of the three different component combinations. This procedure makes it possible to also assign different probabilities to each of the three eddy types and thus results in anisotropic turbulent structures. If all eddy types have the same probability, the flow will be isotropic and capture the original ODT approach. This new approach showed it generality and provides new possibilities of capturing better other anisotropic flows, e. g. wall-bounded flows.

The single-phase HST flow is studied in detail, involving transient statistics and its ODT parameter sensitivity, and is compared with DNS results by Rogers and Moin [49]. The single-phase stationary HST results are presented from $Re_\lambda = 41$ until 269. A wide range of parameter spaces for particle-laden HST are compared to DNS data of Gualtieri et al. [58] and Battista et al. [60]. The model proves its capability to predict these flows quite accurately and to provide extra physical insights to DNS studies. This study concludes the modification of ODT towards a reliable simulation tool to study turbulence modulation caused by particles/droplets and is capable of gathering data for an SGS model.

Submitted to Physical Review Fluids (June 12, 2020).

Division of work: The conceptual work was developed in collaboration with the co-authors. The implementation, simulation execution, and data post-processing were done by me. The paper was written together with all co-authors.

7 Conclusion and Outlook

As a recall from Chapter 1, the aim of this thesis was the investigation of turbulence modulation effects on the gas phase caused by small droplets to provide additional insights in parameter ranges not accessible with DNS.

This aim was reached by extending ODT to enable it to simulate and study turbulence modulation in droplet-laden flows, where the droplets are treated as point-source particles. The extension for spatial, cylindrical flows, the novel approach of the two-way coupling treatment, and a new type of energy redistribution for anisotropic turbulent flows provides ODT with a wide range of new capabilities. In several validation steps against DNS sets of data, ODT could show its reliability to capture physical effects accurately and proved that it can provide extra physical insights beyond the scope of DNS. Additionally, the run time of the simulations is much lower.

The developed framework forms a promising base for several future research paths. For further spray investigations, ODT can be easily extended with an evaporation model to study heat and mass transfer between liquid and gas phase. Furthermore, the drag law can be updated for non-spherical particles and deformations can be considered. Also, the primary break-up model developed by Movaghar [61] can be used as input for poly-dispersed flow simulations. Considering the capability of capturing anisotropic turbulent structures one can also investigate turbulence-modulation in particle-laden wall-bounded flows, which are in particular interest for many industrial applications. Here, it is important to keep in mind the limitation of the reduced dimensionality of ODT capturing only 1D turbulent structures and constraining it to mainly canonical test cases.

Reaching the second aim of contributing to a SGS closure, a new strategy is revealed here how to use ODT data to develop a model for multiphase LES. First investigations could show the importance of the inclusion of such a model. Furthermore, with the promising results achieved with the new ODT framework such a model will provide a significant improvement for multiphase LES.

Appendix: Sub-grid scale model options for LES

Multiphase Direct Numerical Simulations (DNS), which resolve all scales using Eqs. 2.1 and 2.2, are limited to moderately turbulent cases due to their high computational costs [40, 58, 60, 62, 63]. For industrial application with complex geometries, e.g. internal combustion processes in a cylinder, a more affordable simulation tool and still a high accuracy are Large-Eddy-Simulations (LES). LES resolves the larger three-dimensional unsteady turbulent motions and models the small scale motions. The following Chapter gives a very brief summary of the LES procedure with the aim to provide an overview of the sub-grid scale modeling for both single and multiphase flows. A more detailed description of the single phase approach can be found in Pope [12]. Here, the LES framework for multiphase flows was reported by Navarro-Martinez [64].

As nearly all computational costs in DNS are expended on the smallest, dissipative motions, LES provides a reliable alternative for large-scale driven flows. Additionally, the smallest scales are assumed to have, to some extent, a universal character (see Chapter 2.1, Lemma 2), which makes them more suitable for simpler models [12]. The LES procedure is based on a filtering operation, which decomposes the velocity field (u) in a resolved ($\bar{u}$) and a SGS (u^{sgs}) component. The filtered velocity field accounts for 80% of the turbulent kinetic energy in the flow field.

The multiphase LES approach is based on the Σ-Y-PDF method [65, 66]. Here, the joint volume-surface density sub–grid PDF (also known as Filtered Density Function), $P_{sgs}(\mathbf{x}, t, \phi, \Sigma)$ of the liquid volume fraction ϕ, and the surface density Σ is solved using the Eulerian Stochastic Fields method. The full derivation of the equation is reported elsewhere, Navarro-Martinez [64], and here only the final form is shown as

$$\frac{d\phi^\alpha}{dt} + \bar{u}_j \frac{\partial \phi^\alpha}{\partial x_j} = \frac{\partial}{\partial x_j}\left[D_{sgs}\frac{\partial \phi^\alpha}{\partial x_j}\right] + \sqrt{2D_{sgs}}\frac{\partial \phi^\alpha}{\partial x_j} dW_j^\alpha, \tag{7.1}$$

$$\frac{d\Sigma^\alpha}{dt} + \bar{u}_j \frac{\partial \Sigma^\alpha}{\partial x_j} = \frac{\partial}{\partial x_j}\left[D_{sgs}\frac{\partial \Sigma^\alpha}{\partial x_j}\right] + \sqrt{2D_{sgs}}\frac{\partial \Sigma^\alpha}{\partial x_j} dW_j^\alpha + \mathcal{S}_{gen}^\alpha - \mathcal{S}_{des}^\alpha, \tag{7.2}$$

where dW_j^α is a Wiener term of the αth moment with mean 0 and variance equal to $\sqrt{dt}$. The first-moments (or filtered values) are obtained directly by averaging the Stochastic Fields solution. The higher the number of fields the more accurate the representation of the sub-grid scales. $\mathcal{S}_{gen}^\alpha$ and $\mathcal{S}_{des}^\alpha$ are source term, which generate or destroy surface density. The sub-grid diffusivity D_{sgs} requires closure and will be discussed further below.

This system is solved together with the classical filtered Navier–Stokes equation for the one-fluid approach given as

$$\overline{\frac{\partial u_i}{\partial x_i}} = \frac{\partial \bar{u}_i}{\partial x_i} = 0, \tag{7.3}$$

$$\bar{\rho}\frac{\partial \bar{u}_i}{\partial t} + \bar{\rho}\bar{u}_j\frac{\partial \bar{u}_i}{\partial x_j} = \frac{\partial \bar{p}}{\partial x_i} + \bar{\mu}\frac{\partial^2 \bar{u}_i}{\partial x_j \partial x_j} + \frac{\partial \tau_{ij}^{sgs}}{\partial x_j} + \bar{f}_{\sigma,i} + f_{\rho,i}^{sgs} + f_{\mu,i}^{sgs}, \tag{7.4}$$

where τ_{ij}^{sgs} is the unknown SGS stress tensor. $\bar{f}_{\sigma,i}$, $f_{\rho,i}^{sgs}$, and $f_{\mu,i}^{sgs}$ are filtered surface forces and sub-grid interphase forces due to density and viscosity variations, respectively. Their closure is discussed in [67–69] and are not further considered here.

Finding a closure strategy for τ_{ij}^{sgs} and D_{sgs} requires first look into the transport of turbulent kinetic energy between the filtered velocity field and the SGS motions [12]. The filtered energy is decomposed as

$$\bar{E} = E_f + k^{sgs}, \tag{7.5}$$

where $E_f = \frac{1}{2}\bar{u}_i\bar{u}_i$ is the filtered velocity field and k^{sgs} is the SGS kinetic energy. The energy transport equation is given as

$$\frac{\partial E_f}{\partial t} + \frac{\partial}{\partial x_j}\left(\bar{u}_i E_f\right) - \frac{\partial}{\partial x_i}\left(\bar{u}_i\left(\mu\frac{\partial^2 \bar{u}_i}{\partial x_j \partial x_j} - \frac{\partial \tau_{ij}^{sgs}}{\partial x_j} - \frac{\partial \bar{p}}{\partial x_i}\right)\right) = -\epsilon_f - \mathcal{P}_{sgs}, \tag{7.6}$$

where ϵ_f and $\mathcal{P}_{sgs}$ are defined by

$$\epsilon_f = 2\mu\bar{S}_{ij}\bar{S}_{ij}, \tag{7.7}$$

$$\mathcal{P}_{sgs} = -\tau_{ij}^{sgs}\bar{S}_{ij}. \tag{7.8}$$

Whereas the left-hand side of Eq. 7.6 represents the energy transport between resolved and SGS scales, of most interest is the right-hand side. $-\epsilon_f$ represents the viscous dissipation of the filtered velocity field. As discussed in Chapter 2.1, the dissipation is large at the smallest scales and smaller for larger scales in the inertial sub-range as they need to break down further to be transported into thermal energy. Thus, for high-Reynolds number flows with a filter width much larger than the Kolmogorov scales (Eq. 2.11) ϵ_f is relatively small [12]. Contrary $\mathcal{P}_{sgs}$ can be relatively large. It represents the rate of energy transport from the filtered motions to the SGS motions and is, therefore, the main target value for SGS models. Additionally, assuming nearly all energy is captured by the filtered velocity field, the dominant sink term for the overall energy is ϵ, which is nearly equal to the stationary value of $\mathcal{P}_{sgs}$ [12].

In this thesis we consider two options to close τ_{ij}^{sgs}. The most straight forward approach is to provide results directly for $\mathcal{P}_{sgs}$ simulating a particle-laden HST flow configuration. SGS turbulence in LES is governed mainly by the mesh-resolved shear, hence the velocity differences across the coarse-grained control volumes. The periodicity of an HST simulation then corresponds to the control-volume size. The second approach is to modify the commonly used Smagorsiky model [70–72] with data from particle-laden stationary HIT.

In this model, a relation between SGS stress and filtered strain rate is used called linear eddy-viscosity model and given as

$$\tau_{ij}^{sgs} = -2\nu_{sgs}\bar{S}_{ij}. \tag{7.9}$$

The coefficient ν_{sgs} is called eddy viscosity of the SGS motion and depends on state and time. ν_{sgs} in turn is modelled by an analogy of the mixing-length hypothesis as

$$\nu^{sgs} = (C_s\Delta)^2\bar{\mathcal{S}}, \tag{7.10}$$

where C_s and Δ represents the Smagorinsky coefficient and the filter width, respectively. C_s is commonly obtained by using the dynamic approach of Piomelli & Liu [73]. $\bar{\mathcal{S}}$ is the characteristic filtered rate of strain [12]. Using the stationary HIT data requires an modification of Eq. 7.10. Here, we proposed the following based on a dimension analysis and the commonly know $k-\epsilon$ model in RANS.

$$\nu^{sgs} = (C_s\Delta)^2\bar{\mathcal{S}} - C_{ODT}\left(\frac{k_0^2}{\epsilon_0} - \frac{k_p i^2}{\epsilon_p i}\right), \tag{7.11}$$

C_{ODT} is the ODT constant for the turbulence modulation model. The subscript 0 and pi are describing the quantity without and with particle interaction, respectively. The latter will be obtained simulating flows for the local parameter combination of Re_λ, St and ϕ.

The closure of D_{sgs} uses the same scale similarity Smagorisky-type model and is termed as

$$D_{sgs} = \frac{\nu_{sgs}}{Sc_{sgs}}, \tag{7.12}$$

where Sc_{sgs} is the sub-grid Schmidt number, which takes the value of ρ_g/ρ_l in analogy to the RANS mass-weighted model [64]. This relation is also required in case of providing $\mathcal{P}_{sgs}$ data from particle-laden HST, which needs a relation of $\mathcal{P}_{sgs}$ and ν_{sgs}. This is given by combining Eqs. 7.8 and 7.9 to

$$\mathcal{P}_{sgs} = 2\nu_{sgs}\bar{S}_{ij}^2 = \nu_{sgs}\bar{\mathcal{S}}^2. \tag{7.13}$$

References

[1] J. R. Schmidt, J. O. L. Wendt, and A. R. Kerstein, "Non-equilibrium wall deposition of inertial particles in turbulent flow," *J. Stat. Phys.*, vol. 37, pp. 233–257, 2009.

[2] U.S. Energy Information Administration, "International energy outlook 2017. Report No. DOE/EIA-0484.," 2017.

[3] International Energy Agency, "Transport, Energy and CO_2," 2009.

[4] Project Drawdown. https://drawdown.org/solutions/table-of-solutions. Accessed: 2020-04-22.

[5] C. Du, *Studies of Diesel sprays under non-reacting and reacting conditions*. PhD thesis, Chalmers University of Technology, Sweden, 2017.

[6] C. Poelma, *Experiments in particle-laden turbulence*. PhD thesis, TU Delft, Netherlands, 2004.

[7] A. R. Kerstein, "One-dimensional turbulence: model formulation and application to homogeneous turbulence, shear flows, and buoyant stratified flows," *J. Fluid Mech.*, vol. 392, pp. 277–334, 1999.

[8] A. Movaghar, M. Linne, M. Oevermann, F. Meiselbach, H. Schmidt, and A. R. Kerstein, "Numerical investigation of turbulent-jet primary breakup using one-dimensional turbulence," *Intl. J. Multiphase Flow*, vol. 89, pp. 241–254, 2017.

[9] A. Movaghar, M. Linne, M. Herrmann, A. Kerstein, and M. Oevermann, "Modeling and numerical study of primary breakup under diesel conditions," *Intl. J. Multiphase Flow*, vol. 98, pp. 110–119, 2017.

[10] G. Sun, D. O. Lignell, J. C. Hewson, and R. G. Craig, "Particle dispersion in homogeneous turbulence using the one-dimensional turbulence model," *Phys. Fluids*, vol. 26, p. 103301, 2014.

[11] G. Sun, J. C. Hewson, and D. O. Lignell, "Evaluation of stochastic particle dispersion modeling in turbulent round jets," *Intl. J. Multiphase Flow*, vol. 89, pp. 108–122, 2017.

[12] S. B. Pope, *Turbulent Flows*. Cambridge University Press, New York, 2000.

[13] R. Clift, J. R. Grace, and M. E. Weber, *Bubbles, Drops and Particle*. Academic Press, 1978.

[14] C. T. Crowe, J. D. Schwarzkopf, M. Sommerfeld, and Y. Tsuji, *Multiphase Flows with Droplets and Particles*. CRC Press, 2012.

[15] P. Bradshaw and W. A. Woods, *An Introduction to Turbulence and its Measurement*. Pergamon Press, 1971.

[16] L. Davidson, "Fluid mechanics, turbulent flow and turbulence modeling," 2020. Lecture slides, Chalmers TH, Sweden.

[17] A. N. Kolmogorov, "The local structure of turbulence in incompressible viscous fluid for very large reynolds numbers.," *Dokl. Akad. Nauk SSSR*, vol. 30, pp. 299–303, 1941. in russian.

[18] L. F. Richardson, *Weather Prediction by Numerical Process.* Cambridge University Press, New York, 1922.

[19] G. I. Taylor, "Statistical theory of turbulence: Part I-III," *Proc. R. Soc. London Ser. A*, vol. 151, pp. 421–464, 1935.

[20] N. Sharma, "Spray droplet size distribution and droplet velocity measurements in a firing optical engine," *Phys. Fluids*, vol. 32, p. 023304, 2020.

[21] E. Loth, "Quasi-steady shape and drag of deformable bubbles and drops," *Intl. J. Multiphase Flow*, vol. 34, pp. 523–546, 2008.

[22] G. G. Stokes, "On the effect of the internal friction of fluids on the motion of pendulums," *Camb. Phil. Soc.*, vol. 9, pp. 8–106, 1851.

[23] C. W. Oseen, "Über die Stokes'sche Formel und über eine verwandte Aufgabe in der Hydrodynamik," *Ark. f. Mat. Astr. Och. Fys.*, vol. 6, pp. 1–20, 1910.

[24] H. Lamb, "On the uniform motion of a sphere through a viscous fluid," *Phil. Mag.*, vol. 21, pp. 112–121, 1911.

[25] M. T. Landahl and E. Mollo-Christensen, *Turbulence and Random Processes in Fluid Mechanics.* Cambridge University Press, 2 ed., 1992.

[26] NASA, "Drag of a sphere." Website, 2015. https://www.grc.nasa.gov/WWW/k-12/airplane/dragsphere.html, last visit 2020-07-31.

[27] L. Schiller and A. Naumann, "Über die grundlegenden Berechnungen bei der Schwerkraftaufbereitung," *Zeitschrift des Verein Deutscher Ingenieure*, vol. 77, pp. 318–320, 1933.

[28] S. Elghobashi, "Direct numerical simulation of turbulent flows laden with droplets or bubbles," *Annu. Rev. Fluid Mech.*, vol. 51, p. 217–244, 2019.

[29] G. Hetsroni, "Particle-turbulence interaction," *Intl. J. Multiphase Flow*, vol. 15, pp. 735–746, 1989.

[30] E. Achenbach, "Vortex shedding from spheres," *J. Fluid Mech.*, vol. 62, pp. 209–221, 1974.

[31] Y. Tsuji and Y. Morikawa, "LDV measurements of an air-solid two-phase flow in a horizontal pipe.," *J. Fluid Mech.*, vol. 120, pp. 385–409, 1982.

[32] G. Hetsroni and M. Solokov, "Distribution of mass, velocity and intensity of turbulence in a two-phase turbulent jet.," *Trans. ASME Jl appl. Mech.*, vol. 38, pp. 315–327, 1971.

[33] R. Gore and C. T. Crowe, "Effects of particle size on modulating turbulent intensity.," *Intl. J. Multiphase Flow*, vol. 15, pp. 279–285, 1989.

[34] K. D. Squires and J. K. Eaton, "Particle response and turbulence modification in isotropic turbulence," *Phys. Fluids A*, vol. 2, pp. 1191–1203, 1990.

[35] M. Boivin, O. Simonin, and K. D. Squires, "Direct numerical simulation of turbulence modulation by particles in isotropic turbulence," *J. Fluid Mech.*, vol. 375, pp. 235–263, 1998.

[36] A. Ferrante and S. Elghobashi, "On the physical mechanisms of two-way coupling in particle-laden isotropic turbulence," *Phys. Fluids*, vol. 15, pp. 315–329, 2003.

[37] S. Sundaram and L. R. Collins, "A numerical study of the modulation of isotropic turbulence by suspended particles," *J. Fluid Mech.*, vol. 379, pp. 105–143, 1999.

[38] S. Lain and M. Sommerfeld, "Turbulence modulation in dispersed two-phase flow laden with solids from a Lagrangian perspective," *Intl. J. Heat Fluid Flow*, vol. 24, pp. 616–625, 2003.

[39] T. Bosse, L. Kleiser, and E. Meiburg, "Small particles in homogeneous turbulence: Settling velocity enhancement by two-way coupling," *Phys. Fluids*, vol. 18, 2006.

[40] R. Monchaux and A. Dejoan, "Settling velocity and preferential concentration of heavy particles under two-way coupling effects in homogeneous turbulence," *Physical Review Fluids*, vol. 2, pp. 1–16, 2017.

[41] C. Poelma, J. Westerweel, and G. Ooms, "Particle–fluid interactions in grid-generated turbulence," *J. Fluid Mech.*, vol. 589, p. 315–351, 2007.

[42] D. O. Mora, A. Cartellier, and M. Obligado, "Experimental estimation of turbulence modification by inertial particles at moderate Re_λ," *Phys. Rev. Fluids*, vol. 4, p. 074309, 2019.

[43] S. Navarro-Martinez, G. Tretola, M. Yosri, R. Gordon, and K. Vogiatzaki, "An investigation on the impact of small-scale models in gasoline direct sprays (ECN Spray G)," *Intl. J. Eng. Res.*, vol. 21, pp. 217–225, 2019.

[44] D. O. Lignell, V. B. Lansinger, J. Medina, M. Klein, A. Kerstein, H. Schmidt, M. Fistler, and M. Oevermann, "One-dimensional turbulence modeling for cylindrical and spherical flows: Model formulation and application," *Theor. Comp. Fluid Dyn.*, vol. 32, pp. 495–520, 2018.

[45] M. Fistler, "Turbulence-droplet interaction modelled by one-dimensional-turbulence." Lic. thesis, Chalmers TH, Sweden, 2017.

[46] A. R. Kerstein, "Linear-eddy modelling of turbulent transport. Part 6. Microstructure of diffusive scalar mixing fields," *J. Fluid Mech.*, vol. 231, pp. 361–394, 1991.

[47] A. R. Kerstein, W. T. Ashurst, S. Wunsch, and V. Nilsen, "One-dimensional turbulence: Vector formulation and application to free shear flows," *J. Fluid Mech.*, vol. 447, pp. 85–109, 2001.

[48] S. Tavoularis and S. Corrsin, "Experiments in nearly homogeneous turbulent shear flow with a uniform mean temperature gradient. Part 1," *J. Fluid Mech.*, vol. 104, pp. 311–347, 1981.

[49] M. M. Rogers and P. Moin, "The structure of vorticity field in homogenoeus turbulent flows," *J. Fluid Mech.*, vol. 176, pp. 33–66, 1987.

[50] W. T. Ashurst and A. R. Kerstein, "One-dimensional turbulence: Variable density formulation and application to mixing layers," *Phys. Fluids*, vol. 17, p. 025107, 2005.

[51] G. Sun, *Stochastic simulation of Lagrangian Particle transport in turbulent flows*. PhD thesis, Bringham Young University, USA, 2015.

[52] V. Eswaran and S. B. Pope, "An examination of forcing in direct numerical simulations of turbulence," *Comp. Fluids*, vol. 16, pp. 257–278, 1988.

[53] J. R. Schmidt, *Stochastic Models for the Prediction of Individual Particle Trajectories in One Dimensional Turbulence Flows.* PhD thesis, University of Arizona, USA, 2004.

[54] A. R. Kerstein and S. K. Krueger, "Clustering of randomly advected low-inertia particles: A solvable model," *Phys. Rev. E*, vol. 73, p. 25302, 2006.

[55] M. Fistler, D. O. Lignell, A. Kerstein, and M. Oevermann 2020.

[56] S. G. Budilarto, *An experimental study on effects of fluid aerodynamics and particle size distribution in particle laden jet flows.* PhD thesis, Purdue Univeristy, USA, 2003.

[57] A. H. Abdelsamie and C. Lee, "Decaying versus stationary turbulence in particle-laden isotropic turbulence: Turbulence modulation mechanism," *Phys. Fluids*, vol. 24, p. 015106, 2012.

[58] P. Gualtieri, F. Picano, G. Sardina, and C. M. Casciola, "Clustering and turbulence modulation in particle-laden shear flows," *J. Fluid Mech.*, vol. 715, pp. 134–162, 2013.

[59] I. M. Kennedy and M. H. Moody, "Particle dispersion in a turbulent round jet," *Exp. Therm. Fluid Sci.*, vol. 18, pp. 11–26, 1998.

[60] F. Battista, P. Gualtieri, J.-P. Mollicone, and C. M. Casciola, "Application of the Exact Regularized Point Particle method (ERPP) to particle laden turbulent shear flows in the two-way coupling regime," *Intl. J. Multiphase Flow*, vol. 101, pp. 113–124, 2018.

[61] A. Movaghar, *The One-Dimensional Turbulence Model Applied to Spray Atomization.* PhD thesis, Chalmers University of Technology, Sweden, 2018.

[62] M. Tanaka and D. Teramoto, "Modulation of homogeneous shear turbulence laden with finite-size particles," *J. Turb.*, vol. 16, pp. 979–1010, 2015.

[63] A. H. Abdelsamie and C. Lee, "Decaying versus stationary turbulence in particle-laden isotropic turbulence: Heavy particle statistics modifications," *Phys. Fluids*, vol. 25, p. 033303, 2013.

[64] S. Navarro-Martinez, "Large eddy simulation of spray atomization with a probability density function method," *Int. J. Multiphase Flow*, vol. 63, p. 11–22, 2014.

[65] A. Vallet and R. Borghi, "Modelisation eulerienne de l'atomisation d'un jet liquide," *C. R. Acad. Sci - Ser. IIB - Mech. Phys. Astron.*, vol. 327, pp. 1015–1020, 1999.

[66] A. Vallet, A. Burluka, and R. Borghi, "Development of an eulerian model for the atomization of a liquid jet," *Atomization Sprays*, vol. 11, 2001.

[67] M. Gorokhovski and M. Herrmann, "Modeling primary atomization," *Annu. Rev. Fluid Mech.*, vol. 40, pp. 343–366, 2008.

[68] P. Liovic and D. Lakehal, "Multi-physics treatment in the vicinity of arbitrarily deformable gas-liquid interfaces," *J. Comput. Phys.*, vol. 222, pp. 504–535, 2007.

[69] E. Labourasse, D. Lacanette, A. Toutant, P. Lubin, S. Vincent, O. Lebaigue, J.-P. Caltagirone, and P. Sagaut, "Towards large eddy simulation of isothermal two-phase flows: Governing equations and a priori tests," *Int. J. Multiphase Flow*, vol. 33, pp. 1–39, 2007.

[70] J. Smagorinsky, "General circulation experiments with the primitive equation: I. The basic equations.," *Mon. Weather Rev.*, vol. 91, pp. 99–164, 1963.

[71] A. Scotti, C. Meneveau, and D. K. Lilly, "Generalized smagorinsky model for anisotropic grids," 1993.

[72] A. Scotti, C. Meneveau, and M. Fatica, "Dynamic smagorinsky model on anisotropic grids," 1997.

[73] U. Piomelli and J. Liu, "Large-eddy simulation of rotating channel flow using a localized dynamic model," 1995.